Environment International 186 (2024) 108610

Contents lists available at ScienceDirect

Environment International

journal homepage: www.elsevier.com/locate/envint

Full length article

Submicron aerosol pollution in Greater Cairo (Egypt): A new type of urban haze?

Aliki Christodoulou [a,b,*], Spyros Bezantakos [a], Efstratios Bourtsoukidis [a], Iasonas Stavroulas [a,c], Michael Pikridas [a], Konstantina Oikonomou [a], Minas Iakovides [a], Salwa K. Hassan [d], Mohamed Boraiy [e], Mostafa El-Nazer [f], Ali Wheida [f], Magdy Abdelwahab [g], Roland Sarda-Estève [h], Martin Rigler [i], Giorgos Biskos [a], Charbel Afif [a,j], Agnes Borbon [k], Mihalis Vrekoussis [a,l,m], Nikos Mihalopoulos [a,c], Stéphane Sauvage [b], Jean Sciare [a]

[a] Climate and Atmosphere Research Center (CARE-C), the Cyprus Institute, Nicosia, 2121, Cyprus
[b] IMT Nord Europe, Institut Mines-Télécom, Univ. Lille, Centre for Energy and Environment, 59000 Lille, France
[c] Institute for Environmental Research and Sustainable Development, National Observatory of Athens, Athens, Greece
[d] Air Pollution Research Department, Environment and Climate Change Research Institute, National, Research Centre, El Behooth Str., Giza 12622 Dokki, Egypt
[e] Physics and Mathematical Engineering Department, Faculty of Engineering, Port Said University, Port Said, Egypt
[f] Theoretical Physics Department, Physics Institute, National Research Centre, El Behooth Str., Giza 12622 Dokki, Egypt
[g] Astronomy and Meteorology Department, Faculty of Science, Cairo University, Cairo, Egypt
[h] Laboratoire Des Sciences Du Climat Et de l'Environnement (LSCE), CNRS-CEA-UVSQ, Gif-sur-Yvette, France
[i] Research and Development Department, Aerosol D.o.o., Ljubjana, Slovenia
[j] Emissions, Measurements, and Modeling of the Atmosphere (EMMA) Laboratory, CAR, Faculty of Science, Saint Joseph University, Beirut, Lebanon
[k] Laboratoire de Météorologie Physique, UMR6016, Université Clermont Auvergne, OPGC, CNRS, 63000 Clermont-Ferrand, France
[l] University of Bremen, Institute of Environmental Physics and Remote Sensing (IUP), Germany
[m] Center of Marine Environmental Sciences (MARUM), University of Bremen, Germany

ARTICLE INFO

Keywords:
Megacity
Submicron aerosols
Urban haze
Greater Cairo
Hygroscopic aerosols
Ammonium Chloride

ABSTRACT

Greater Cairo, the largest megacity of the Middle East North Africa (MENA) region, is currently suffering from major aerosol pollution, posing a significant threat to public health. However, the main sources of pollution remain insufficiently characterized due to limited atmospheric observations. To bridge this knowledge gap, we conducted a continuous 2-month field study during the winter of 2019–2020 at an urban background site, documenting for the first time the chemical and physical properties of submicron (PM_1) aerosols. Crustal material from both desert dust and road traffic dust resuspension contributed as much as 24 % of the total PM_1 mass (rising to 66 % during desert dust events), a figure not commonly observed in urban environments. Our observations showed significant decreases in black carbon concentrations and ammonium sulfate compared to data from 15 years ago, indicating an important reduction in both local and regional emissions as a result of effective mitigation measures. The diurnal variability of carbonaceous aerosols was attributed to emissions emanating from local traffic at rush hours and nighttime open biomass burning. Surprisingly, semi-volatile ammonium chloride (NH_4Cl) originating from local open biomass and waste burning was found to be the main chemical species in PM_1 over Cairo. Its nighttime formation contributed to aerosol water uptake during morning hours, thereby playing a major role in the build-up of urban haze. While our results confirm the persistence of a significant dust reservoir over Cairo, they also unveil an additional source of highly hygroscopic (semi-volatile) inorganic salts, leading to a unique type of urban haze. This haze, with dominant contributors present in both submicron (primarily as NH_4Cl) and supermicron (largely as dust) modes, underscores the potential implications of heterogeneous chemical transformation of air pollutants in urban environments.

* Corresponding author.
E-mail address: a.christodoulou@cyi.ac.cy (A. Christodoulou).

https://doi.org/10.1016/j.envint.2024.108610
Received 4 November 2023; Received in revised form 24 February 2024; Accepted 26 March 2024
Available online 27 March 2024

1. Introduction

The growth of urban populations and the consequent rise in anthropogenic activities lead to deteriorating air quality, which, in turn, has significant direct and indirect adverse impacts on public health and climate. According to the World Health Organization (WHO, 2021) and the European Environment Agency (EEA, 2023), short and long-term exposure to high concentrations of gaseous and particulate air pollutants is related to various health issues, such as irritated eyes, headaches, asthma, strokes and chronic diseases of the cardio-respiratory system (e.g., Lelieveld et al., 2019). Several epidemiological studies have demonstrated the impact of particulate matter (PM) on human health with increased mortality and morbidity (Ain & Qamar, 2021; Arias-Pérez et al., 2020; Dockery & Pope, 1996; Kelly & Fussell, 2012; Marey et al., 2010; Martinelli et al., 2013). All these effects are likely to be exacerbated in megacities, which concentrate both high pollution levels and high exposure levels to this pollution.

Monitoring and characterizing the sources and properties of particulate matter and gaseous pollutant levels in megacities is consequently critical for a better assessment of their health impacts and also for evaluating the efficiency of applied air pollution mitigation measures, including new strategies to control emissions from specific sources.

The WHO's revised air quality guidelines established more stringent annual (5 μg m^{-3}) and 24-hour (15 μg m^{-3}) limits for $PM_{2.5}$ that reflect the evolving understanding of their health impacts at lower concentrations (WHO, 2021). Yet, there's a notable absence of PM_1 regulations, highlighting a gap in public health policy. Addressing this gap by expanding research and regulations to include PM_1 is crucial for protecting public health from air pollution.

The focus on PM_1 has been limited, despite evidence pointing to its severe health effects, partly due to the scarcity of measurements. Emerging studies highlight the urgent need to address PM_1 in epidemiological research, showing strong associations between fine particles and lung cancer mortality, which emphasizes the danger of even smaller particles (Chen et al., 2017; Franck et al., 2011; Lin et al., 2016).

The Eastern Mediterranean and Middle East (EMME) region has been identified as an air pollution hotspot (Osipov et al., 2022) with major influence of long-range transported air masses originating from three continents, Europe, Asia (Middle East), and Africa (Lelieveld et al., 2002), therefore comprising a mixture of natural and inadequately controlled anthropogenic emissions (Kanakidou et al., 2011; Lelieveld et al., 2002; Pikridas et al., 2018; Vrekoussis et al., 2005, 2022). The EMME experiences enhanced regional background pollution levels, particularly during summer, leading to exceedances of ozone and PM thresholds (Gerasopoulos et al., 2006; Kanakidou et al., 2011; Kleanthous et al., 2014). Therefore, air quality in EMME cities is not only impacted by local emissions but also by its regional background levels (e.g., Christodoulou et al., 2023) and intense pollution episodes emanating from distant sources. Eventually, the adverse health impact of air pollution in EMME cities may also be amplified by extreme weather events (e.g., heat waves). The latter is of significant importance as the EMME region is identified as a major hotspot for climate change (Mostafa et al., 2019; Zittis et al., 2019, 2022).

The Greater Cairo (GC) megacity, the capital of Egypt, stands as the largest city in the EMME region. Its population exceeds 22 million inhabitants according to the Central Agency for Public Mobilization and Statistics (CAPMAS), contributing to a national population of approximately 110 million. In such gigacity regions, haze from mixed anthropogenic and natural sources can strongly influence the planetary boundary layer (PBL) (Ding et al., 2016; Huang et al., 2020; Z. Wang et al., 2018), resulting in the formation of extensive heat and pollution islands (Kulmala et al., 2021). A characteristic example of such conditions is the Indo-Gangetic Plain (IGP), where numerous observational studies focusing on surface PM concentrations have been conducted over India during the past decade. For instance, Gunthe et al. (2020 and references therein) reported persistently high chloride in Delhi and episode spikes in chloride concentrations in Chennai. These authors suggested that in the presence of excess ammonia in Delhi, high local emission of hydrochloric acid partitions into aerosol water. The highly water-absorbing and soluble chloride in the aqueous phase substantially enhances aerosol water uptake through co-condensation, which sustains particle growth, leading to haze and fog formation. Several rapidly urbanizing areas in Africa (like Cairo), are likely to undergo similar developments (Chen et al., 2020; Hoornweg & Pope, 2017; Ramaswami et al., 2016). However, detailed studies on the chemical composition of fine particles are missing at these gigacities.

According to the report by the World Bank (2012), Cairo is recognized among the most polluted cities globally, while Cheng et al. (2016) ranked Cairo as the second most heavily polluted city concerning $PM_{2.5}$ levels among 45 megacities, following Delhi (India). Most of the studies conducted over the past decades, in Cairo have provided only partial information on the PM levels, composition, and sources (Abbass et al., 2020; Abu-Allaban et al., 2002, 2007; El-Metwally et al., 2008; Favez et al., 2008; Zakey et al., 2008) with very few documenting all the major PM chemical components such as carbon, ions, and trace metals (e.g. Abu-Allaban et al., 2002; 2007; Favez et al., 2008; Lowenthal et al., 2013). Moreover, most of these measurements were performed 10 to 20 years ago. Therefore, they can no longer account for the current air pollution in Cairo, and assess the efficiency of new environmental policies and the adoption of cleaner technologies, alongside the substantial growth in population over recent years (Heger et al., 2019).

To the best of our knowledge, there have been no studies conducted in Greater Cairo concerning the submicron aerosol (PM_1), which is a crucial component of PM contributing to haze formation with severe health implications (Chen et al., 2017; Hu et al., 2022; Gunthe et al., 2021). In addition, all PM measurements conducted so far in GC have used filters to collect PM, which are known to suffer from sampling artifacts (e.g., absorption/desorption of semi-volatile aerosol species) and lack of high-time resolution (hour or less) that can provide valuable insights on the diurnal variability of PM components and the dynamic of their emission sources.

To advance this limited knowledge on the actual chemical composition and sources of PM in GC and better assess its influence on air quality and health we conducted the field campaign POLCAIR (Air Pollution in Greater Cairo: sources and impact) project. This two-month intensive field campaign, spanning from November 28, 2019, to January 29, 2020 (prior to the COVID-19 lockdown), was carried out at a residential site representative of urban background conditions in GC.While, both online and offline measurements of the chemical and physical properties of aerosols were performed in this campaign, this work is more focused on the chemical composition and hygroscopicity of submicrometer aerosols in order to better assess their haze formation potential.

2. Methodology

2.1. Site description

Atmospheric measurements in the frame of the POLCAIR project were performed in Cairo, the capital city of the Arab Republic of Egypt, located at the base of the Nile Delta, (Fig. 1a).

A comprehensive suite of state-of-the-art aerosol instrumentation was deployed at the premises of the National Research Centre of Egypt (NRC; 30.0358° N, 31.2051° E). The sampling site is located approximately 3.5 km southwest of the city center (Fig. 1b), 1 km west of the Nile river, and 1 km north of the Cairo University, the latter being used as a sampling site by Favez et al. (2008). All instruments were installed on the rooftop of a six-floor building with a clear (360°) unobstructed view. The site was chosen as representative of the Greater Cairo urban area (Fig. 1b), where urban-related emission sources can be observed with minimal local traffic contamination (the closest major roads being located at 250 m distance).

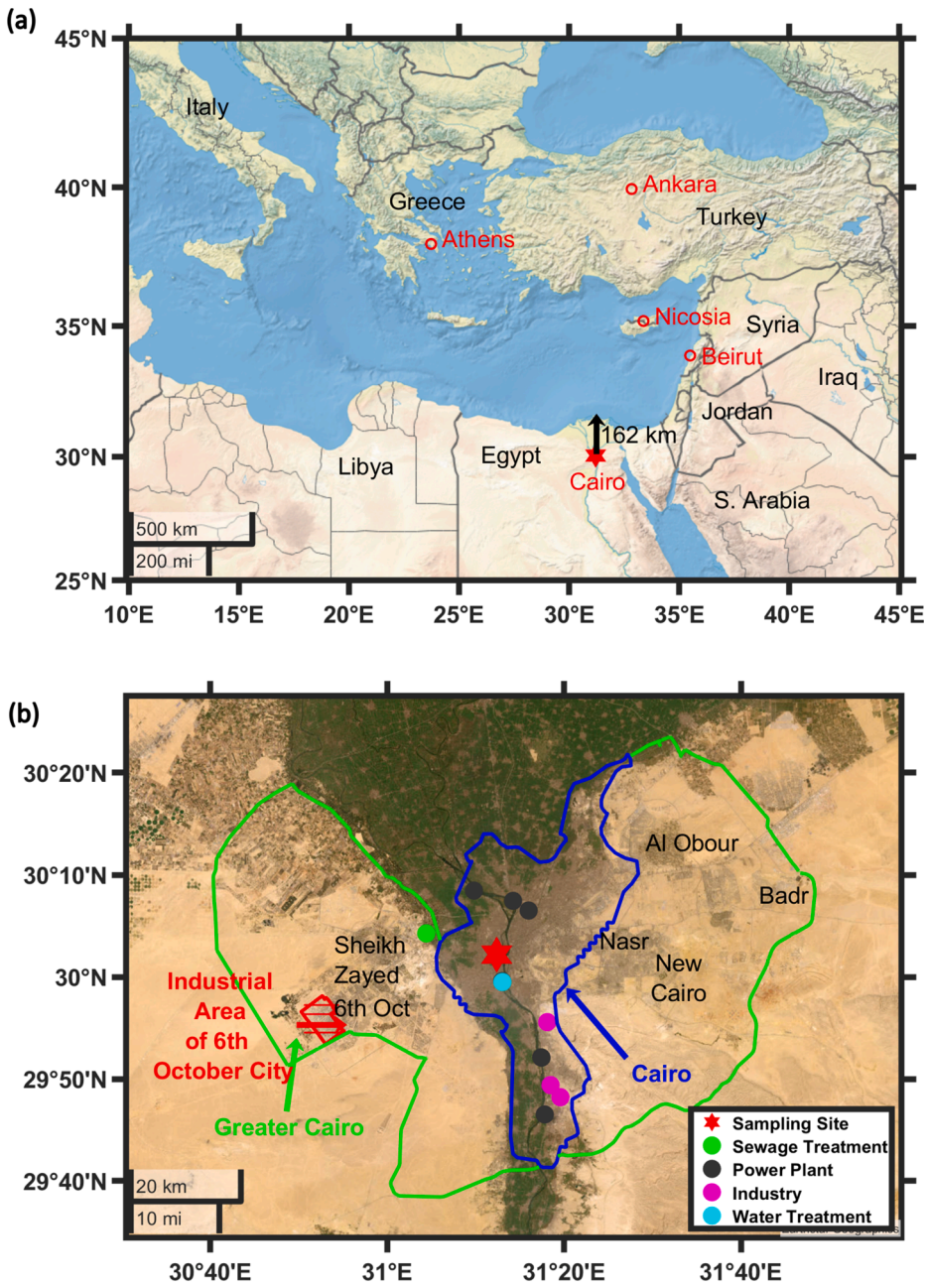

Fig. 1. (a) Location of the Greater Cairo megacity in the Eastern, (b) Location of the measurement site (red star) within the Cairo (blue line) and Greater Cairo (green line) urban area. Location of major sewage and water treatment plants, power plants, and industries are also shown (Source: google maps). (For interpretation of the references to color in this figure legend, the reader is referred to the web version of this article.)

2.2. Timelines

The field campaign started on November 27th, 2019, and ended on January 29th, 2020, resulting in more than two consecutive months of continuous observations (80–95 % coverage) before the COVID-19 lockdown (Spring of 2020) and Muslim Ramadan (23rd April to 23rd May 2020). The timing of the campaign, which mostly covered the winter season, was chosen as a period of the year with minimal influence of biomass burning, which occurs in the Nile Delta around October (Mahmoud et al., 2008; Marey et al., 2010; Prasad et al., 2010) and dust storms which typically occur in Spring (El-Metwally et al., 2011). Therefore, the observations are expected to enable an optimal characterization of local city emissions with potentially less interference from nearby emission sources.

2.3. Instrumentation

The instrumentation deployed during the campaign is described in Table 1 for each aerosol parameter, along with the related instrument/technique, averaged time resolution, and period of operation. Reactive and greenhouse gas measurements were also performed to identify their primary/secondary sources and will be further exploited in a separate publication.

Submicron aerosol composition (NR-PM$_1$: Non-refractory PM$_1$). Measurements were performed continuously using a quadrupole aerosol chemical speciation monitor (Q-ACSM, Aerodyne Research Inc., USA). The instrument provides quantitative information for non-refractory species such as organics, nitrate, sulfate, ammonium, and chloride in the size range of ca. 40–1300 nm; 90 – 650 nm with more than 50 % penetration efficiency vacuum aerodynamic diameter; (Liu et al., 2007;

Table 1
Aerosol Measurements and Instruments at the sampling site.

Parameter	Instrument	Time resolution	Measuring Period (data points /samples, data coverage)
Chemical Characterization of Non-Refractory PM_1	Q-ACSM	29 min	28/11/2019 – 29/01/2020 (3019 data points, 100 %)
Black Carbon (BC)	Aethalometer A33/	1 min	28/11/2019 – 29/01/2020 (89 k data points, 100 %)
PM_1 Filter sampling (EC/OC, Ions, Metals)	Leckel SEQ 47/50	6 h	02/12/2019 – 28/01/2020 (225 filter samples, 85 %)
Submicron aerosol Hygroscopic properties	HTDMA	6 min	04/12/2019–28/01/2020 (19265 hygr. distributions / 5 dry mobility diameters, 60 %)
Submicron particle mobility size distribution	SMPS	5 min	04/12/2019–28/01/2020 (12056 size distributions, 69 %)
Meteorological Parameters	Vaisala Weather station WXT 536	5 min	01/12/2019 – 28/01/2020 (16 k data points, 95 %)

Ng et al., 2011). Data were retrieved using ACSM local v.1.6.0.3 software, implemented in Igor Pro (v. 6.37, Wavemetrics Inc., USA). To account for incomplete detection caused by particle bounce, the mass concentrations were corrected using the chemical composition-dependent collection efficiency (CDCE) method (Middlebrook et al., 2012). The corresponding parameters, response factor (RF), and relative ionization efficiency (RIE) are reported in Table S1. More details about the Q-ACSM setup, operation, and QA/QC protocol used here can be found in Christodoulou et al. (2023).

Black Carbon (BC): Continuous black carbon (BC) mass-equivalent concentration measurements were obtained using a dual spot, 7-λ Magee Scientific AE-33 aethalometer (Drinovec et al., 2015), operated at a flow rate of 3 L min^{-1} and a 1-min time resolution. The "Aethalometer model" (Sandradewi et al., 2008) was used to allocate contributions of biomass burning (BC_{bb}) and fossil fuel combustion (BC_{ff}) to BC concentrations. The model calculates the fractional biomass burning contribution based on light absorption coefficients recorded at 470 and 950 nm and assuming instrument-default Ångström Absorption Exponents of 1.0 and 2.0 for fossil fuel combustion and biomass burning, respectively. The instrument was equipped with a PM_1 cut-off inlet (BGI Inc., USA) and a Nafion dryer.

Aerosol number size distribution: The aerosol number size distribution in the range of ca. 14–680 nm was measured by a commercially available SMPS system (Wang & Flagan, 1989), consisted of a long DMA (TSI Inc. model 3081), its control unit (TSI Inc. model 3080) and a condensation particle counter (CPC; TSI Inc. model 3025; Stolzenburg & McMurry, 1991). The system was operated at a sheath-to-aerosol ratio of 10:1 (i.e., 3 and 0.3 L min^{-1}, respectively) while being equipped with a silica diffusion dryer and a soft X-ray neutralizer (TSI Inc. model 3088) to ensure adequate drying and neutralization of the sampled aerosols. The raw measurements were inverted into number-size distributions with a resolution of 64 channels/decade using the manufacturer's software (TSI AIM ver. 9c), also used for multiple charge correction.

Aerosol hygroscopicity: A custom-made HTDMA (Rader & McMurry, 1986) system, similar to the one described in more detail in Salmatonidis et al. (2020), was employed for measuring the hygroscopic growth factors of monodisperse aerosols having electrical mobility diameters of 30, 60, 90, 120 and 160 nm (**cf. supplement Section1 for more details**). The sampling interval was 3 min for each monodisperse dry electrical mobility diameter, while the total measuring cycle for all 5 dry mobility diameters was 30 min (i.e., two consequent measurements for each dry mobility diameter).

The inverted size distributions were fitted with a custom-made algorithm (Bezantakos et al., 2013) to calculate the geometric mean electrical mobility diameter of the humidified particles, which in turn was used for deriving their hygroscopic growth factor (**cf. supplement Section1 for more details**). In addition, the algorithm is capable of distinguishing between internally and externally mixed aerosol populations (pronounced by wider/bimodal distributions at elevated RH conditions).

The measured hygroscopic growth factors were then converted to the respective single hygroscopic parameters "κ". Note that in the case of externally mixed aerosols, more than one "κ" value can be calculated, with each one denoting the hygroscopicity of each population. Sampled particles were conditioned and charged by the dryer and the neutralizer of the SMPS.

PM_1 Filter collection for off-line chemical composition determination: Off-line measurements were carried out to collect particles every 6 h (4 samples per day from midnight local time) onto 47-mm diameter quartz filters (Pall Gellman, TISSUQUARTZ) using a low-volume sampler (Leckel SEQ47/50) operating at a flow rate of 2.3 m^3/h. During the 2-month campaign period, 225 filters were collected continuously. The elemental/organic carbon (EC/OC) content was analyzed using a Sunset OC/EC lab analyzer following the EUSAAR2 thermal protocol described in (Cavalli & Putaud, 2010). Major anions and cations were analyzed using ion chromatography (Bimenyimana et al., 2023; Sciare et al., 2008) after extraction of filter punches in ultrapure water. PM_1 samples were additionally analyzed for trace elements (A, Fe, Ca, Zn, Pb, Cu, Ni, V, Cr, Mn, Cd, and As) by Inductively coupled plasma mass spectrometry (ICP-MS) based on the method described in Bimenyimana et al. (2023).

Meteorological parameters: Standard meteorological parameters (temperature, relative humidity, wind speed, and direction) were obtained from a meteorological station located near the sampling station.

Air masses back-trajectory analysis: Air mass 72-hour retroplumes were modeled using the FLEXible PARTicle (FLEXPART) dispersion model (Pisso et al., 2019) in backward mode. Particles (n = 40,000) were released from 350 m a.g.L. and followed back in time for 3 days (Stohl et al., 2002) using as input three-dimensional forcing datasets from the NOAA Climate Forecast System (CFS) short-duration (t < 6 h) forecasts (Saha et al., 2014). In this work, only the lower 100 m a.g.L., as representative of the interaction of the receptor site with local sources, were considered.

3. Results and discussion

3.1. Meteorological conditions

During the two months of the POLCAIR campaign, the meteorological conditions encountered were relatively stable from one day to another and variable within the day (see Fig. 2 & Fig. S1). Although the campaign was performed during winter, the sampling period was characterized by mild and typical temperatures for the period (on average at 15.4 ± 3.2 °C) (The World Bank Group). The observed range of Relative Humidity (RH) varied from 45 to 75 % over the day, being atypically high for a city located near desertic regions. However, this can be explained for Cairo by the presence of the Nile river and intense agriculture activities (incl. irrigation) in the Nile delta, which, together with elevated temperatures, promote intense evaporation. These humid conditions are likely to promote condensation of liquid water onto hygroscopic aerosols and, therefore, contribute to the degradation of visibility, which is often observed over Cairo over the first hours of the day (Fig. 3 & Fig. S1).

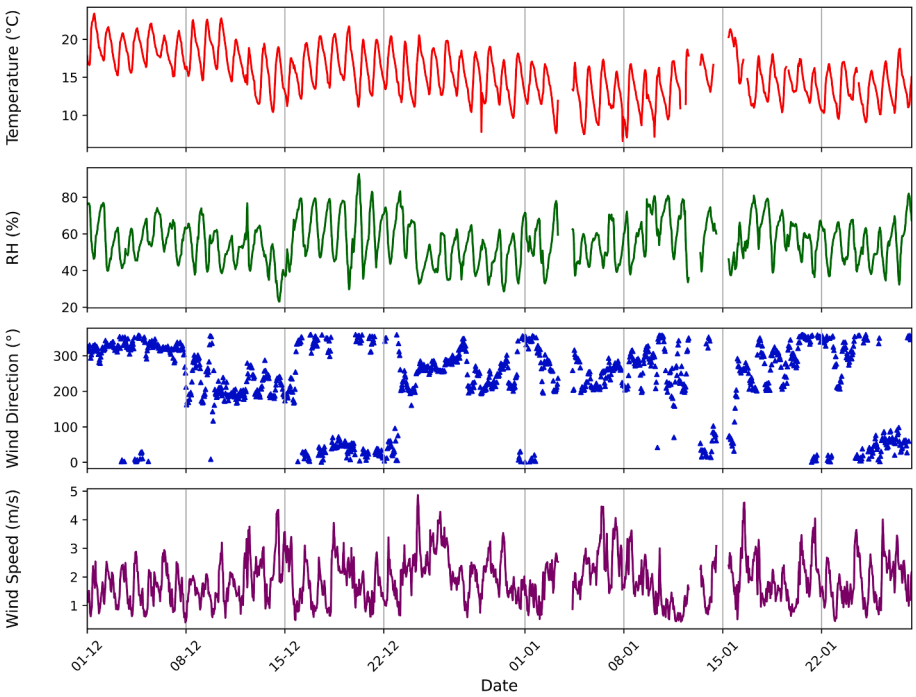

Fig. 2. Temporal variability of temperature, RH, Wind speed, and Wind direction during the POLCAIR campaign.

Fig. 3. South view of the sampling site in the morning and afternoon, highlighting the diurnal change of visibility along the day.

The sector distribution of winds for the campaign duration, depicted in Fig. S2, clearly shows the predominance of NW winds during most days, followed by W and SW directions mainly during the night and until sunrise. Exceptions to this pattern occurred only on the few days when the wind direction was pointing from the sector between N and NE (Fig. 2).

3.2. Air masses origin

Figure S3 shows the seven clusters of back-trajectory classes calculated for the 2-month campaign. During this period, GC was mostly influenced by air masses originating from southeast Mediterranean Sea (cluster 1–2 with contribution 13–22 % respectively) (Fig. S4a), northeast Mediterranean Sea (Aegean Sea, close to Turkish coastline, west of Turkey) (cluster 3–4 with respective contribution 22 – 14 %) (Fig. S4b) and the central Mediterranean Sea, south of Italy (cluster 7 contributing 9 %) (Fig. S4c). Although the major air masses arriving in Cairo originated from the Mediterranean Sea, two important clusters were identified originating from northwest Africa (clusters 5 and 6 with relative contribution of 11 and 9 %, respectively) and mostly covered by the Saharan Desert (Fig. S4d). In the following sections, the analysis of these two distinctive air mass episodes will further be explored.

Apart from the previously discussed seven clusters, it's worth noting that specific periods exhibited predominant air masses originating from the Middle East, encompassing countries like Lebanon, Syria, Iraq, Israel, Saudi Arabia, and Turkey (Fig. S4 a–d), and were associated with prevailing north-to-northeast winds passing over the Nile Delta region (Fig. 2). These events will also be further discussed in the following.

3.3. Fine (PM_1) aerosol chemical composition

3.3.1. Comparison between online and offline measurements of individual chemical species

Ammonium, sulfate, nitrate, and chloride concentrations measured with the Q-ACSM (i.e., in the PM_1 size fraction) were averaged throughout the sampling duration of the off-line PM_1 (filter) measurements. Direct comparisons were made, resulting in correlations with more than 200 data points covering a wide concentration range of at least an order of magnitude (Fig. S5 a–e). Overall, all elements show a very strong correlation, including chloride, which is usually underestimated by filter sampling because of the volatility of NH_4Cl (Budisulistiorini et al., 2014; Witz et al., 1990). The observed slopes were 1.13

with $R^2 = 0.93$ for SO_4^{2-}, 1.03 with $R^2 = 0.94$ for NH_4^+, 1.11 with $R^2 = 0.96$ for NO_3^- and 1.04 with $R^2 = 0.89$ for Cl^-. Measurements marked with a circle (sulfate in Fig. S5b and organics in te potential interference from dust concentrations and correspond to values where calci **Fig. S5a**) indicaum concentrations exceed 6 μg m^{-3}.

The concentrations of organic aerosols (OA) are also compared to the OC levels determined on PM_1 filters. An excellent agreement is also found here ($R^2 = 0.89$), with a slope of 1.6, similar to the one used to reconstruct chemically the PM_1 mass, and being close to the values reported by Christodoulou et al. (2023) for Nicosia (Cyprus) during wintertime and OM/OC calculations from AMS measurements in polluted environments (Saarikoski et al., 2012).

Given the excellent agreement between the Q-ACSM observations (NR-PM_1 components) and PM_1 filters, in the following discussion inorganic and OM levels derived from Q-ACSM will be used, while PM1 filters will be used for the estimation of dust and trace elements.

Dust calculation

The calculation of fine mode crustal mass (dust) was done by using the trace elements levels determined on PM_1 filters (Table S2) and by implementing the IMPROVE formula (Malm et al., 1994), similar to other studies (e.g., Pant et al., 2015). This formula uses the oxides of the main soil elements such as Al_2O_3, SiO_2, CaO, FeO, Fe_2O_3, and TiO_2 to calculate dust concentration as follows:

$$[Dust] = 2.20*[Al] + 2.49*[Si] + 1.63*[Ca] + 2.42*[Fe] + 1.94*[Ti] \quad (2)$$

Silicon in (Eq. (2)) cannot be directly measured by ICP-MS but was estimated here using an Al to Si ratio of 0.45 (Simon et al., 2011). Fig. 4 represents the reconstructed chemical composition in PM_1. On average, the fractions of major chemical species followed the order: ions (mainly sulfate, nitrate, ammonium, and chloride, i.e., SIA), OM, dust, EC, and Trace Elements (TE) accounting for 38 %, 30 %, 24 %, 6 %, 2 % respectively (Fig. 4 s subplot).

Intense dust episodes have the potential to temporarily influence PM concentrations and composition. An important dust event was observed during the campaign between 25 and 26/12, marked by a peak in PM_{1chem} concentration of almost 150 μg m^{-3} (Fig. 4). During this period, dust contributed to ca. two-thirds of the total PM_{1chem}. This result is noteworthy as it showcases that dust can become the predominant species in PM_1 in Cairo, a fraction that otherwise is usually attributed to anthropogenic emissions.

However, removing the contribution of this 'major' dust event, the relative contribution of the various chemical species to PM_1 is only marginally changed by 2–3 %, with dust remaining the third contributor to PM_1 load. This finding indicates that dust is likely to be ubiquitous in Cairo even in PM_1.

Trace Elements: Data on trace elements measured in this work are depicted in Table S2 and compared with the values reported in the literature in Table S3. It is important to note that due to the absence of previous research focusing on PM_1 in Cairo, comparisons are constrained to studies based on filter $PM_{2.5}$ and PM_{10} fractions. Nevertheless, for elements of anthropogenic origin, mainly confined in the fine fraction, such comparisons, despite potential limitations, can offer valuable insights. For instance, for lead (Pb) and cadmium (Cd), a comparison with literature data (Table S3) revealed a decrease of more than an order of magnitude, indicative of effective mitigation strategies applied in the last 20 years. As shown in Table S3, Pb has gradually and continuously decreased by a factor of five in 10 years, from ca. 1000 ng m^{-3} in 2000–2001 to ca. 200 ng m^{-3} in 2010 (Zakey et al., 2008; Lowenthal et al., 2013). These results suggest that Pb has further decreased between 2010 and 2019 (down to 127 ng m^{-3}, this study) although at a slower pace. Levels of Pb, Cd, arsenic (As), and nickel (Ni) levels are comparable to the values reported for GC in the period of 2018 (Monged et al., 2022).

3.3.2. *Reconstruction of online submicron PM_1*

The sum of the concentrations of chemical components measured by the Q-ACSM and the BC concentrations measured by the Aethalometer cannot be compared directly with PM_{1chem} since any of these two online

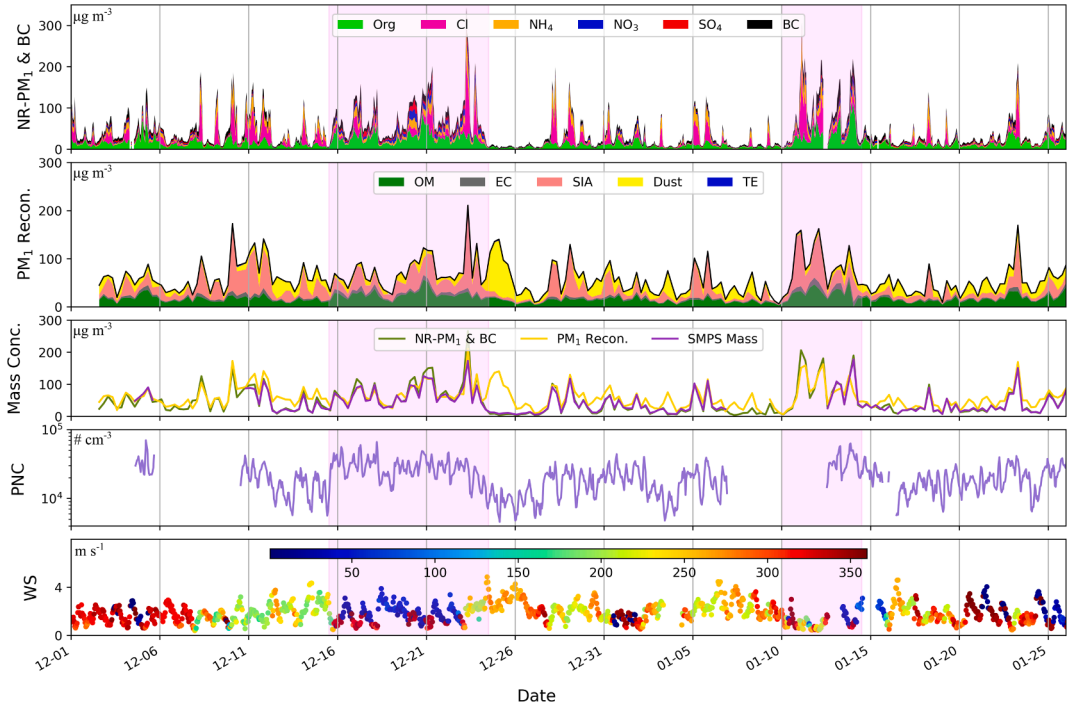

Fig. 4. Time series of 1-hour average NR-PM_1 species measured by the Q-ACSM (first subplot) and Black Carbon concentrations (1-hour average) measured by the aethalometer (black line, first subplot), Time series of PM1 reconstructed mass measured by filters (6-h average) (second subplot), Mass concentration of NR-PM1&BC; PM1 Reconstructed; SMPS deconvolved mass (third subplot), Particle Number Concentration (PNC) measured by SMPS (logarithmic y-axis, forth subplot) and Wind Speed (WS) color-plotted with wind direction for the entire measuring period (fourth subplot). Purple-shaded areas refer to the two pollution episodes (PP1 & PP2) observed during the campaign. (For interpretation of the references to color in this figure legend, the reader is referred to the web version of this article.)

instruments measured dust, which has shown to account on average for 24 % of PM_{1chem}. Alternatively, this sum was compared with PM mass concentration derived by the SMPS. This direct comparison is possible considering the size range of the SMPS (up to 0.7 μm diameter) and that of the Q-ACSM, while accounting for the transmission efficiency of the aerodynamic lenses of the Q-ASCM (Liu et al., 2007) and expressing the electrical mobility diameters to vacuum aerodynamic ones. This comparison shows a strong correlation coefficient $R^2 = 0.95$ and a slope very close to unity (1.09, see Fig. S5f), when an apparent density of the particles of 1.6 g cm^{-3} is assumed, further validating the consistency of online chemical measurements. Additionally and even more importantly, both correlation coefficient and slope suggest that the PM fraction with diameters below 0.7 μm does not contain a significant amount of dust, which can be detected by the SMPS if present within its measuring range. This outcome further implies that most of the dust in PM_1 likely falls within the 0.7–1 μm range, potentially as a submicron extension of the larger (supermicron) mode.

Fig. 4 illustrates the time series of NR-PM_1 components (Org, Cl, NH_4, NO_3, SO_4) from Q-ACSM, BC as measured by the aethalometer, PM_1 chemical composition from filters, and the Particle Number concentration (PNC) measured by SMPS, along with selected meteorological parameters (wind direction and speed) for the duration of the campaign.

3.3.3. Concentration of chemical species

The campaign's average for hourly-resolved NR-PM_1 is 40.05 ± 40.32 μg m^{-3}, ranging from 2 to 324 μg m^{-3} with a median value of 24.96 μg m^{-3} (±indicates the standard deviation reflecting the variability of the measurement over the averaged period). It is interesting to note that the sum of NR-PM_1 (40.05 μg m^{-3}) with BC (7.25 μg m^{-3}), filter-based dust (12.3 μg m^{-3}), and trace elements (0.95 μg m^{-3}) gives a total of 60.6 μg m^{-3} which is very close to the 59.6 μg m^{-3} calculated for the reconstructed PM_{1chem} over the campaign, further cross-validating both online and off-line measurements.

The hourly maximum NR-PM_1 concentrations were observed on 23rd December (323 μg m^{-3}). Overall, NR-PM_1 was dominated by organic aerosols (OA), which accounted for 42 % of the total NR-PM_1, followed by chloride 25 %, ammonium 16.6 %, nitrate 9 %, and sulfate 6 % (Table S4). Table 2 showcases results from studies in other large cities, including those in the East Mediterranean. These studies incorporate both BC and Q-ACSM measurements, allowing for a direct comparison with the present work. The levels observed in our study significantly exceed the WHO guidelines for 24-hour $PM_{2.5}$ concentrations. While such high concentrations of PM_1 have been recorded in urban centers in China and India, they are notably lower than those reported in previous studies from this region, as shown in Table 2.

As already emphasized for filter-based OC, the prevalence of submicron OA in Cairo aligns with findings from previous studies conducted worldwide (Chen et al., 2022a; Sun et al., 2016; Zhou et al., 2018). However, reports on EC and OC concentrations in Cairo have been limited, with only two studies by Favez et al (2008) and Abu-Allaban et al. (2007), presenting results from collected filters at TSP and $PM_{2.5}$ fractions, respectively. In particular, the study by Favez et al. (2008) provides urban background measurements obtained close to the location of this study and conducted over extended periods, including annual and winter season data for three consecutive years. The findings reveal a distinct declining trend in organic carbon (OC) and elemental carbon (EC) concentrations over 15 years (i.e., by factors of 2 and 3, respectively). Conversely, the levels reported by Abu-Allaban (2007) although at different seasons indicate a significant decrease only for EC (factor of 2).

The sulfate concentrations are usually representative of a regional (than local) background. While the measured concentrations are a factor of 2 to 5 lower compared to those reported 20 years earlier in Cairo (Table S5), they are consistent with those observed recently in the Mediterranean (Kaskaoutis et al., 2023). However, the high contribution of NH_4^+ and specifically of Cl^- is not often observed in the literature. Only a few limited studies in India have reported such high concentrations and contributions of chloride in NR-PM_1 (Gani et al., 2019; Reyes-Villegas et al., 2021) (Table 2). By considering the strong association of NH_4^+ with Cl^- ($R^2 = 0.93$), NH_4Cl contributes to almost half (41 %) of the total NR-PM_1 mass, becoming thus the most abundant component even when compared to organics, which represents a huge number of compounds. In addition, the average Cl/Na ratio of 26.55 calculated over the entire measurement period is about 15 times greater than their typical ratio in seawater (1.8) and indicates significant contributions from anthropogenic sources. Interestingly, our non-sea-salt chloride concentrations are similar to those reported by Favez et al. (2008) (all year-round measurements) and Abu-Allaban (2007) for Cairo, suggesting no important decrease in emissions for this compound over the last two decades (see Table S5).

3.3.4. Factors controlling the variability of online chemical species

To further examine the influence of sources and chemical processes on the variability and composition of NR-PM_1, we divided this large dataset into seven clusters using different criteria (Fig. 5 & Table S6). The first two subsets of data accounted for day and night time conditions. Daytime, defined as the hours between 6:00–18:00 (LT), corresponding to periods of sunshine, while nighttime, from 19:00 to 05:00 LT, encompassed dark hours. Two more data clusters were created to explore the factors controlling the high and low loadings of NR-PM_1, respectively. The first subset, named 'HL' (High Loading), included NR-PM_1 concentrations exceeding 100 μg m^{-3}, while the second subset, 'LL'

Table 2
Comparison of concentrations of the main submicron chemical species derived by ACSM for different cities in the region and the world. BC derived by Aethalometer measurements.

City (Country)	Type of site	Period	OA	SO_4^{2-}	NO_3^-	NH_4^+	Cl^-	NR-PM_1	BC	Reference
			Mean [μg m^{-3}]							
Cairo (Egypt)	Urban	Dec-Jan	16.7	2.6	3.9	6.8	9.9	40.05	7.25	This Study
Beijing (China)	Urban	Jun-Aug	20	9	3.5	5.5	0.5	50.0	–	Sun et al., 2012
Hong-Kong (China)	Urban	Sep-Dec	15	6	1.8	2.8	0.3	25.9	–	Sun et al., 2016
Delhi (India)	Urban	Feb	40	3.9	3.7	4.5	6	58.1	–	R.-Villegas et al., 2021
Delhi (India)	Urban	Winter	112	16	24	20	23	195	15	Gani et al., 2019
Nicosia (Cyprus)	Suburban	Winter	5.03	2.81	1.22	1.14	0.14	10.30	2.01	Christodoulou et al., 2023
Athens (Greece)	Urban	Winter	9	2.5	1.2	0.9	0.15		2.4	Stavroulas et al., 2019

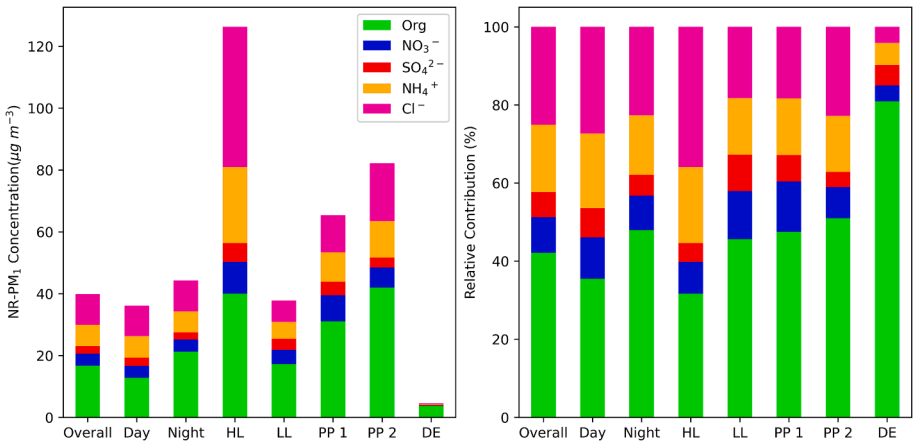

Fig. 5. NR-PM_1 concentration and relative contribution during different subsets/clusters of the campaign. HL, LL = High and Low Loading periods, PP1, PP2, DE = Pollution episode 1, Pollution episode 2, Dust event, respectively. (High Loading periods: NR-PM_1 mass > 100 μg m^{-3} & Low Loading periods: NR-PM_1 mass < 100 μg m^{-3}).

(Low Loading), included concentrations below 100 μg m^{-3}. This differentiation was made due to the presence of shorter pollution episodes lasting only a few hours or up to a day, in addition to the two primary pollution episodes. Following these, two more clusters/subsets refer to the two pollution episodes (PP1, PP2). Finally, the last subset corresponds to a period impacted by dust.

DAY-NIGHT: Daytime and nighttime averages are 35.67 μg m^{-3} (±41.89 μg m^{-3}) and 44.33 μg m^{-3} (±37.85 μg m^{-3}), respectively (Fig. 5). These datasets show slightly higher NR-PM_1 concentrations at night but the overall chemical composition remains with quite similar contributions of organics and NH_4Cl (around 40 %) and a slight increase of organics over the night.

HL-LL: During the periods with high loadings, NH_4Cl appears as the dominant contributor, with more than half of NR-PM_1. During the same periods, organics exhibit the lowest relative contribution of around 30 %, suggesting that NH_4Cl is a major driver of PM_1 pollution events in Cairo. Conversely, during periods with low loadings, organics are the dominant species (around 48 %), suggesting a permanent (urban) background contribution of carbonaceous aerosols.

DE: The dust event shows the lowest NR-PM_1 concentrations among the 7 clusters, which can be partly explained by a higher ventilation rate (wind speed during the dust event was above average; Fig. 4) but also by lower RH, which is likely to play an important role on the formation of NH_4Cl (see later on).

PP1-PP2: Two pollution periods (PP) were observed during the campaign and are associated with intense and long-lasting haze/smog events. Pollution period 1 (PP1) started on 15/12/2019 and ended on 25/12/2019 (first shaded area in Fig. 4), whereas pollution period 2 (PP2) started on 10/01/2020 and ended on 14/01/2020 (second shaded area in Fig. 4). Both episodes occurred under meteorological conditions when the prevailing winds had north to north-east origin (i.e., passing over the Nile delta) and corresponded to the two periods with air masses, primarily originating from the Middle East (See Fig. S4e–h). PP1 had an average value of NR-PM_1 of 65.37 μg m^{-3} and recorded the highest hourly concentrations (above 300 μg m^{-3}) for NR-PM_1 during the campaign, with organics (32 %) and chloride (19 %) comprising its major fraction. During PP2, an average NR-PM_1 value of 82 μg m^{-3} and a maximum hourly concentration during the first days of the episode to almost 300 μg m^{-3} were measured. The average OA mass concentration (41.93 μg m^{-3}) and contribution (almost 51 %) were higher in PP2 than in PP1. However, the percentage contribution of sulfate in PP2 decreased, as depicted in Fig. 5, from 6.7 % in PP1 to 3.9 % in PP2, indicating the possible difference in the origin of the air masses. Contrary to sulfate, the contribution of chloride increased largely in PP2, from 18.3 % in PP1 to 22.9 % in PP2. The relative contribution of ammonium between the two periods was similar to 14–15 %. Thus, although an increase in organics is observed, NH_4Cl contributes almost equally with organics in PP1 and dominates in PP2 (Fig. 5).

Overall, independently of the air masses origin and wind direction NH_4Cl is a great contributor to total NR-PM_1.

3.3.5. *Diurnal variability of NR-PM1 species*

The diurnal variations of NR-PM_1 species and BC during the entire campaign are shown in Fig. 6.

Sulfate: Sulfate is the only compound that does not display strong diurnal variations, with the highest concentrations observed during 06:00–12:00 LT and the lowest during 14:00 – 20:00 LT. The relatively flat pattern seen in the diurnal variability of sulfate is commonly reported in the literature and can be attributed to its regional origin, although we can distinguish higher concentrations in the late morning-midday that can be attributed to the photochemical (heterogeneous) processing of gas phase SO_2, as reported by Khoder (2002) and Hassan et al. (2013) in one of the suburban areas of Cairo.

Black Carbon: Black Carbon shows a double peak in the morning and the evening. The highest concentration was observed early morning at 07:00 LT, reaching levels as high as 13.4 ± 9.6 μg m^{-3}, and the lowest one in the afternoon at 14:00 LT (3.3 ± 1.7 μg m^{-3}), probably combined with the dilution effect of the higher boundary layer during this time. This diurnal variability of BC is mainly dictated by its fossil fuel component (BC_{ff}), which exhibits the typical double peak usually attributed to traffic at rush hours in the morning and evening. These observations are in line with the Cairo traffic congestion times, as reported by Nakat et al. (2013).

On the other hand, BC from biomass burning (BC_{bb}) shows a different pattern with persistent high concentrations (around 1 μg m^{-3}) for almost the entire nighttime, when it usually shows an evening peak and low values over the night in many European cities during wintertime. While BC_{bb} concentrations are much lower compared to BC_{ff}, it is important to note that these two sources have very different OC/EC ratios, with $(OC/EC)_{bb}$ likely to be up to a factor of 10 higher compared to $(OC/EC)_{ff}$ over Cairo (Favez et al., 2008 and references therein). As such, while BC_{ff} may be 4–5 times higher compared to BC_{bb}, OC_{bb} may be similar or even higher compared to OC_{ff}.

Organics: Three peaks are observed in the diurnal variability of organic compounds: one at 2:00 (LT) (22.4 ± 20.9 μg m^{-3}) which is very rarely observed within urban environments, a second at 8:00 LT (18.6 ± 14.8 μg m^{-3}), and a third at 21:00 LT (23.9 ± 18.5 μg m^{-3}). This observation supports the earlier assumption of a significant fraction of organics originating from biomass burning (in phase with the nighttime BC_{bb}) and traffic-related sources (in phase with the double peaks of

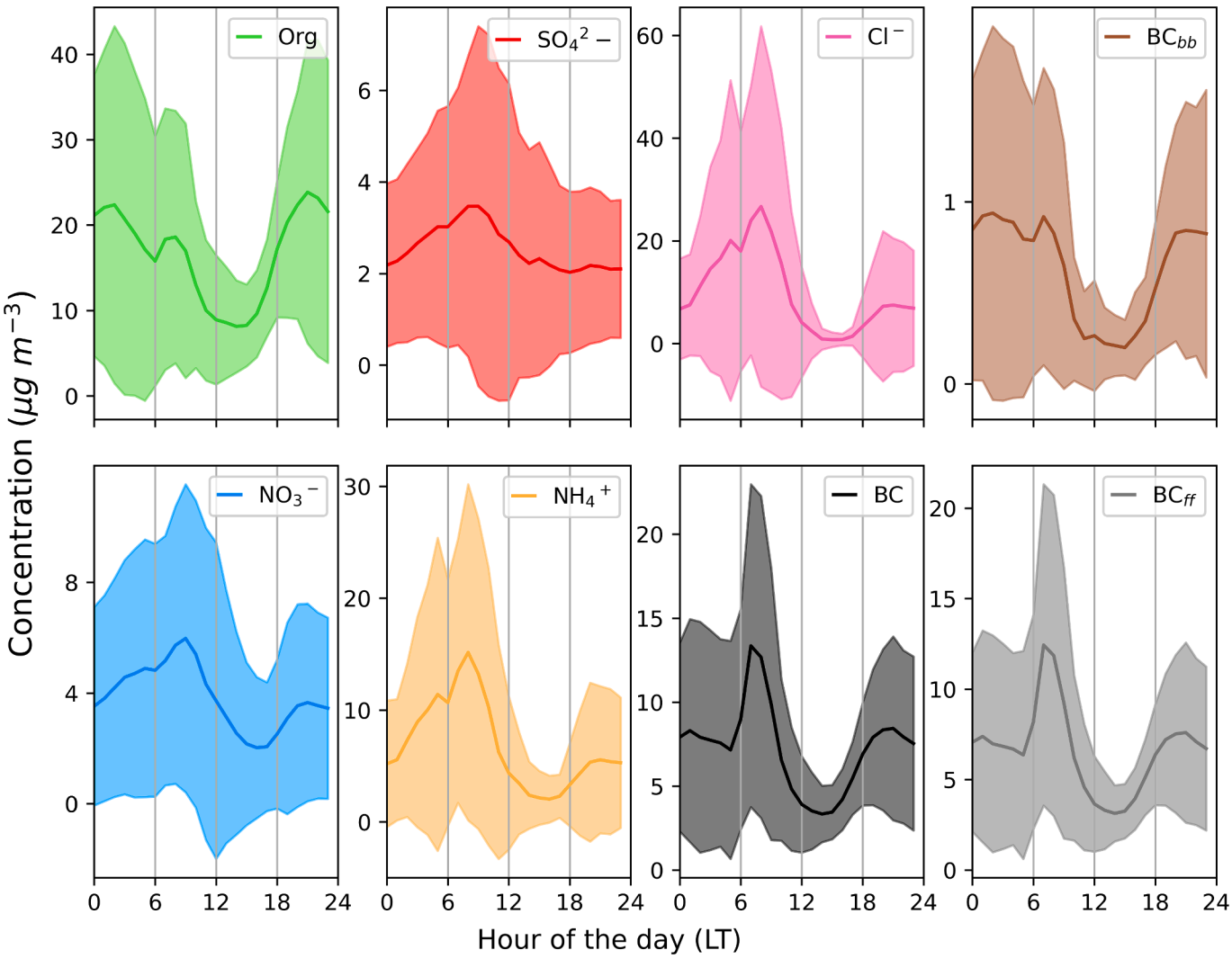

Fig. 6. NR-PM_1 species & BC (BCbb, BCff) diurnal variability. The thick lines represent the means and the shaded areas span the standard deviation.

BC_{ff}). The presence of three peaks in organic compounds is likely the result of a combination of these two major sources. It also demonstrates the value of high-time resolution measurements performed in our study to apportion the variability of combustion sources over Cairo.

Nitrate: The diurnal variation of NO_3^- reflected optimal thermodynamic conditions to form ammonium nitrate and coincided with the traffic hours (with 2 2-hour delay in the morning maximum at 09:00 LT and late evening at 22:00 LT). Being in the form of semi-volatile NH_4NO_3, condensation of nitrate is likely to be promoted by high relative humidity that will keep nitrate in the liquid phase and prevent its volatilization despite mild temperatures (e.g., the role of liquid water content on semi-volatile NH_4NO_3 in Beijing (Sciare et al., 2007).

Chloride: As for nitrate, chloride showed higher concentrations between 2:00 to 10:00 (LT). At 8:00 (LT), the chloride fraction reached its maximum, together with organics, with an hourly average of 26.7 ± 35.1 μg m^{-3}. At 15:00 (LT), chloride contributed very little to the total NR-PM_1 mass with diurnal average concertation below 0.7 ± 1.4 μg m^{-3}. Its variation is similar to that reported in New Delhi and other Indian cities in winter (Gunthe et al., 2021; Reyes-Villegas et al., 2021). Under favorable thermodynamic conditions, the formation of NH_4Cl results from the condensation of both NH_3 and HCl as follows:

$$NH_3 + HCl \rightarrow NH_4Cl \quad (3)$$

To better elucidate the factors affecting NH_4Cl formation and stabilization in the aerosol phase, its diurnal variability was plotted together with RH for selected conditions (i.e., full period, non-event, PP1; see Fig. 7b & Fig. S6). Chloride presented the same diurnal variability during all studied events, co-variating with RH, indicating stabilization in liquid phase (under elevated ambient RH conditions) in agreement with the thermodynamic behavior of NH_4Cl (Gunthe et al., 2021). The impact of ambient RH is also depicted in Fig. 7a presenting the variability of the Cl/PM_1 mass ratio as a function of RH and shows a clear increase of the Cl contribution to PM_1 mass for RH > 50 %.

The significant contribution of NH_4Cl to PM_1 mass, especially at RH above 50 %, together with its highly hygroscopic capacity, will substantially enhance aerosol water uptake through co-condensation, which will sustain particle growth, enhance aerosol condensation sink of reactive gases, therefore further leading to haze formation (Gunthe et al., 2021; Chen et al., 2022b).

3.4. Insights on the sources of dust and ammonium chloride

Dust: The calcium concentrations in PM_1 in this study are remarkably higher (by a factor of 10) than the ones reported in Abu-Allaban et al. (2007) for $PM_{2.5}$. On the other hand, the calcium concentration in PM_1 (this study) is consistently lower (by a factor of 3–4) than those reported for PM_{10} by Favez et al. (2008). As expected, calcium measured in this study correlates mainly with elements of crustal origin (Al, Fe, Mn, Ti; Fig. S7). This finding, coupled with the disparities in dust concentrations in $PM_1/PM_{2.5}/PM_{10}$ mentioned above, underscores the need

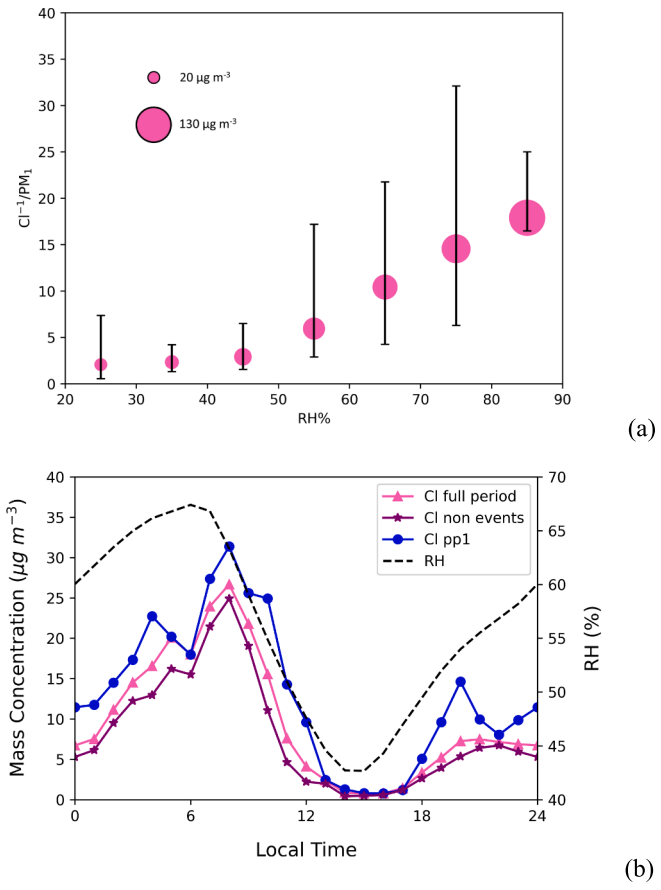

Fig. 7. Median chloride mass fraction in dry PM_1 as a function of RH. The size of the circle indicates PM_1 dry mass concentration. The error bars represent the 25th and 75th percentile (a). Diurnal profile of chloride concentrations in pink line for the entire period, purple for non-event periods, and blue for pollution episode 1 PP1, with a dashed line marking RH on the right y-axis. (For interpretation of the references to color in this figure legend, the reader is referred to the web version of this article.)

for further in-depth analysis of dust composition and sources in PM as it may not solely originate from natural (desert) sources. This is indicated by the fact that the average contribution of dust in PM_1 remains significant, comprising 21 % of the total PM_1 mass concentration even when excluding the major dust event of the 25th of December. More specifically, dust characterization may warrant special attention since mitigation measures to decrease re-suspended dust from traffic may pose challenges to be implemented in Cairo, where natural dust deposition is expected to be substantial and washing out of the streets by rain may be particularly low. Equally important, the continuous high loading of dust in PM_1 indicates a much higher loading in $PM_{2.5}$ and PM_{10}, thereby representing an important sink of water vapor and of a range of inorganic species as reported by Favez et al. (2008). In addition, coarse dust particles can act as a sink for sub-micrometer aerosols due to coagulation (Hinds, 1999), especially when the number concentration of the coarse mode is high, e.g. during a dust event (Jung et al., 2002). Coagulation of hygroscopic sub-micrometer aerosols on coarse dust particles can increase their water affinity (Tsai et al., 2015) and consequently their condensation sink potential. The reduction of the sub-micrometer particle number concentration (PNC; cf. Fig. 4) during the major dust event (DE) can be explained by their coagulation with the coarse dust particles in combination with the higher ventilation rate conditions prevailing during the DE (see section 3.3.4). Therefore, dust can be a significant contributor of urban haze observed over Cairo by acting as condensation and coagulation sink for atmospheric water, inorganic species and sub-micrometer aerosols.

Ammonium chloride: As discussed in Section 3.3.5, the high levels of NH_4Cl (i.e., the most abundant chemical species in PM_1) are attributed to the condensation of gas-phase ammonia and hydrochloric acid. The Nile Delta constitutes a significant agricultural ammonia hotspot, as confirmed by satellite observations (Clarisse et al., 2009; Van Damme et al., 2018), bringing to Cairo elevated levels of NH_3. In their global emission inventory of HCl and particulate chloride from continental sources, Zhang et al. (2022) reported that emissions of HCl are mostly from open waste burning (38 %), open biomass burning (19 %), energy (19 %), and residential (13 %) sectors. The major contribution of open waste burning and open biomass burning on HCl was further assessed by D. Goetz et al. (2018) who reported emission factors for these specific combustion sources (open garbage burning and agricultural residue), highlighting large amounts of chloride from both sources but also high levels of organics and black carbon.

The concentration hotspots for chloride and ammonium shown in the polar plot (Fig. S8d–e) differ from those of other chemical species (Fig. S8a–c), as they point towards the south of the city. Although the hotspot aligns with a high concentration of chloride in the morning, this is also when thermodynamic conditions are favorable (high RH) for its formation, thus not implying a direct link to wind direction from the south. Instead, this suggests that waste burning activities, contributing to these concentrations, are widespread across the region, rather than being localized to the southwest (Fig S6.).

The potential role of open waste burning and open biomass burning over Cairo has been reported in the literature (e.g., Favez et al., 2009; Mahmoud et al., 2008). It is consistent with the statement that solid waste burning constitutes a major source of pollution in Greater Cairo (World Bank Group, 2012). The city generates 9.5 million tons of municipal solid waste annually, accounting for 47 % of the municipal waste generated in Egypt, with collection coverage ranging between 40 and 90 % in urban areas. A large amount of this waste (about 83 %) ends up in large open dumps, and the remainder accumulates in streets or on illegal dumping sites. Five percent is being disposed of in sanitary landfills. As such, waste management seems inefficient and inadequate in Cairo, and self-ignition and open burning are regular patterns on these sites (ElSaid & Aghezzaf, 2018).

The significant correlation observed between NH_4, Cl, and K (Fig. S7) (a well-known tracer of biomass burning) indicates that open burning practices of both municipal solid waste and biomass may happen at the same time and/or result from the mix of these two sources. Since, NH_4Cl is a highly hygroscopic species it is theoretically predicted that the presence of NH_4Cl in the particle phase, at important levels as such observed in this work, will enhance aerosol hygroscopicity (Petters and Kreidenweis, 2007).

3.5. *Submicron particle hygroscopicity (HTDMA)*

Fig. 8 shows the hourly averaged hygroscopic parameters derived by the HTDMA measurements (i.e., "κ_{HTDMA}") of aerosols having dry mobility diameters of 30 and 160 nm, while for rest of the sampled sizes are provided in Fig. S9. The majority of the sampled monodisperse aerosol populations (i.e., above 86 % of the measured samples) exhibited an externally mixing state, resulting in two distinct hygroscopic modes after being exposed to elevated RH levels (i.e., ca. 89 %), which is typical for particles sampled in urban areas (Swietlicki et al., 2008). For this reason, the number fraction of the particles residing in each hygroscopic mode is also denoted by different colors in Fig. 8 and Fig. S9. Aggregated results showing the campaign mean values and standard deviations of the hygroscopic parameters and number fractions of each hygroscopic mode for each dry monodisperse aerosol population, together with the percentage of samples exhibiting externally mixed behavior, are given in Table 3. Overall, all examined monodisperse aerosol populations exhibited a hydrophobic/nearly hygroscopic mode with average κ_{HTDMA} values of ca. 0.1 and a more hygroscopic one with average κ_{HTDMA} values of more than ca. 0.3 (see Table 3). However, the

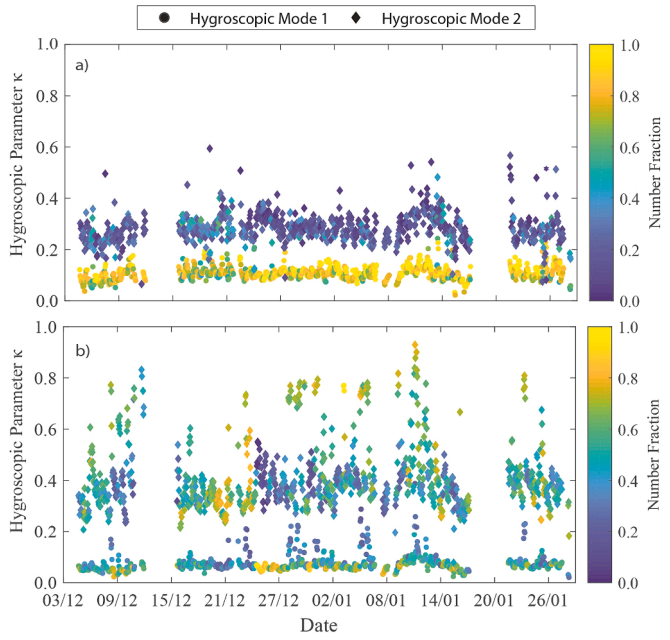

Fig. 8. Hourly averaged hygroscopic parameter kappa values of particles having dry electrical mobility sizes of 30 (a), and 160 (b) nm. Kappa values were obtained from the respective hygroscopic growth factors (i.e., HTDMA measurements) accounting for the mixing state (i.e., internal or external) of the sampled aerosols. Different symbols represent the different observed hygroscopic modes (i.e., externally mixed aerosols), while the colors denote the number fraction of particles residing in each hygroscopic mode.

Table 3
Aggregate results of particle hygroscopic parameters κ and mixing state during the POLCAIR campaign for the different dry mobility diameters sampled by the HTDMA. For each sampled dry mobility diameter, the average values and standard deviations (in parenthesis) of the measured hygroscopic parameter and the number concentration fraction for each mode (i.e., κ_{mode1}, κ_{mode2} and N_{f1}, N_{f2}, respectively) are provided. In addition, the percentage of samples where externally mixed particles were observed (i.e., with coexistence of two hygroscopic modes) is denoted with P_{ex}.

D_{dry} (nm)	κ_{mode1}	N_{f1}	κ_{mode2}	N_{f2}	P_{ex} (%)
30	0.11 (0.03)	0.83 (0.14)	0.28 (0.06)	0.18 (0.14)	86.4
60	0.08 (0.03)	0.62 (0.17)	0.30 (0.09)	0.38 (0.17)	98.9
90	0.08 (0.03)	0.54 (0.17)	0.34 (0.11)	0.46 (0.18)	99.8
120	0.07 (0.04)	0.53 (0.18)	0.37 (0.12)	0.47 (0.18)	99.9
160	0.08 (0.05)	0.52 (0.18)	0.41 (0.13)	0.48 (0.18)	99.3

number fraction of aerosols residing in each hygroscopic mode differed significantly for each monodisperse population measured. In more detail, the vast majority (i.e., number fraction of 83 %) of the aerosols having a dry electrical mobility diameter of 30 nm resided in the hydrophobic/nearly hygroscopic mode, while only 52 % of those with a dry electrical mobility diameter of 160 nm resided in the same hygroscopic mode. In addition, the hygroscopicity of the sampled aerosols classified as more hygroscopic increased as their dry electrical mobility diameters increased. For instance, the maximum hygroscopicity of the aerosols with dry electrical mobility diameters of 30 and 60 nm rarely exceeded the value of 0.6, while that of the aerosols with dry electrical mobility diameters of 160 nm exhibited maximum values above 0.9. This increasing trend is also reflected in the campaign average hygroscopic parameter values exhibited by the particles residing in the more hygroscopic mode (Table 3).

Since the hygroscopic parameter of the sampled aerosols depends on their chemical composition (Petters and Kreidenweis, 2007), certain conclusions can be derived from the HTDMA measurements. The majority of the hydrophobic and less hygroscopic chemical species (i.e., BC and organics having κ values 0 and ca. 0.1, respectively) formed a distinct hygroscopic mode (i.e., hydrophobic/nearly hygroscopic) being externally mixed from other more hygroscopic chemical species with most of them residing in the lower sizes of the aerosol distribution (i.e., 30 and 60 nm exhibiting number fractions of 83 and 62 % for the hydrophobic/nearly hygroscopic mode). While the same distinct mode (i.e., hydrophobic/nearly hygroscopic mode) with similarly low hygroscopicities was observed for aerosols of larger sizes (i.e., 90, 120, and 160 nm), only half of those resided in this mode. The other half of the population of these larger aerosols exhibited hygroscopicities indicative of mixtures of highly hygroscopic species (e.g., atmospheric salts like ammonium sulfate and/or chloride) with less hygroscopic species (i.e., BC and/or organics) at various proportions or even at certain cases hygroscopic properties related only to pure highly hygroscopic species (i.e., κ_{HTDMA} values above 0.5; which is the value of pure ammonium sulfate). Most strikingly, κ_{HTDMA} values close to unity were observed for the largest particles sampled with the HTDMA, indicative of ammonium chloride having a theoretically derived κ value of ca. 0.95 according to the Extended AIM Aerosol Thermodynamics model (E-AIM model 4, Friese & Ebel, 2010; Wexler & Clegg, 2002) or in the order of 0.75, if the volatility and partial evaporation of the ammonium chloride aerosols inside the HTDMA apparatus is taken into account (D. Hu et al., 2011). This finding not only corroborates the existence of ammonium chloride, observed by the online and offline aerosol chemical composition measurements but also suggests that in certain instances such as during high loading periods and pollution events, ammonium chloride particles formed a distinct population (i.e., externally mixed) from other aerosols of the same size. In more detail, while the hygroscopicity of 30 nm aerosols remained rather unchanged throughout the different subsets (i.e., HL, LL, PP1, PP2, Day, Night; see section 3.3.4), the one exhibited by their bigger counterparts (i.e, 160 nm) classified in the more hygroscopic group, showed significant variations (see. Table 4). In addition,

Table 4
Aggregate results of particle hygroscopic parameters κ and mixing state during the different subsets/events for particles having dry mobility diameters of 30 and 160 nm. For each sampled dry mobility diameter, the average values and standard deviations (in parenthesis) of the measured hygroscopic parameter and the number concentration fraction for each mode (i.e., κ_{mode1}, κ_{mode2} and N_{f1}, N_{f2}, respectively) are provided. In addition, the percentage of samples where externally mixed particles were observed (i.e., with coexistence of two hygroscopic modes) is denoted with P_{ex}.

$d_{m,dry}$	*Event*	κ_{mode1}	N_{f1}	κ_{mode2}	N_{f2}	P_{ex} %)
30 nm	HL	0.11 (0.02)	0.74 (0.15)	0.30 (0.05)	0.26 (0.15)	97
	LL	0.11 (0.03)	0.83 (0.14)	0.28 (0.06)	0.17 (0.14)	86
	PP1	0.11 (0.03)	0.75 (0.15)	0.30 (0.05)	0.25 (0.15)	96
	PP2	0.12 (0.03)	0.85 (0.14)	0.33 (0.06)	0.15 (0.14)	81
	Day	0.11 (0.03)	0.85 (0.13)	0.29 (0.07)	0.15 (0.13)	82
	Night	0.10 (0.02)	0.77 (0.15)	0.28 (0.05)	0.23 (0.15)	94
160 nm	HL	0.11 (0.06)	0.34 (0.11)	0.50 (0.21)	0.67 (0.11)	100
	LL	0.07 (0.02)	0.54 (0.17)	0.39 (0.10)	0.46 (0.17)	100
	PP1	0.07 (0.02)	0.47 (0.22)	0.36 (0.09)	0.53 (0.22)	98
	PP2	0.09 (0.04)	0.47 (0.14)	0.46 (0.15)	0.53 (0.14)	100
	Day	0.08 (0.03)	0.52 (0.19)	0.41 (0.12)	0.48 (0.19)	99
	Night	0.07 (0.03)	0.51 (0.17)	0.39 (0.12)	0.49 (0.17)	100

the number fraction of the 160-nm particles which were classified as more hygroscopic was found increased during periods of elevated chlorine mass concentrations (i.e., P1 and P2) and significantly increased during the HL period where NH_4Cl dominated NR-PM_1 (see section 3.3.4). Overall, elevated chlorine mass concentrations are associated with an increase in the hygroscopicity of the bigger particles sampled by the HTDMA (e.g., those having dry mobility diameters of 160 nm) and were classified as more hygroscopic, as theoretically predicted and shown in Fig. S10.

Favorable conditions for the formation of particulate NH_4Cl, like elevated RH (see section 3.3.5), in combination with its very high water affinity can promote condensation of water vapor on the particles, favoring haze formation as demonstrated by Gunthe et al. (2021) and Chen et al. (2022b). The possibility of haze formation under elevated ambient RH conditions is significantly higher when these highly hygroscopic aerosols are observed in high number concentrations (i.e., denoted by the number fraction of the more hygroscopic mode; e.g., during HL event). We should note, that the frequent observations of accumulation mode particles (i.e., 120 and 160 nm) exhibiting hygroscopicities close to that of pure NH_4Cl, is indicative of their local origin and distinct source, since these aerosols did not had enough time to coagulate or participate in atmospheric processing to be mixed with other species.

4. Conclusions

In the framework of the POLCAIR field campaign, a detailed characterization of the chemical and physical properties of submicron (PM_1) aerosols at an urban background site of Greater Cairo (Egypt) was performed. Continuous observations, covering a 2-month period of the winter 2019–2020, were obtained using a comprehensive suite of quality controlled off-line and online atmospheric measurements.

The submicron particulate matter exhibited strong variability of its number concentration, with hourly averaged number concentrations reaching as high as 70 x 10^3 #/cm^3 during intense pollution events. Analysis of aerosol hygroscopicity, which, depends on chemical composition, revealed that submicron aerosols in Cairo were externally mixed, exhibiting two modes: i) a hydrophobic/less hygroscopic mode indicating significant contributions of species such as organics and BC, and ii) a more hygroscopic one that is consistent with mixtures of less hygroscopic species (e.g., organics) with more hygroscopic ones (e.g., ammonium chloride, sulfate, nitrate). Interestingly, highly hygroscopic aerosols (i.e., more hygroscopic than pure ammonium sulfate), exhibiting hygroscopicities similar to that of ammonium chloride were observed in certain cases (e.g., during high loading periods and pollution episodes), forming a distinct population (i.e., externally mixed), accounting for 60 % of the number concentration of the bigger particles (i.e., 120 – and 160 – nm; in dry conditions).

All these observations point to strong variability and heterogeneity of the observed sub-micron aerosols, indicative of the different sources and processes which were further assessed from a detailed characterization of submicron aerosol chemical properties.

Carbonaceous aerosols were measured as OC and EC from filter-based measurements, BC from biomass burning (BC_{ff}) and fossil fuels (BC_{bb}) from an aethalometer, and organics from Q-ACSM.

The most important findings of the study are the following:

- EC and OC were correlated, suggesting that combustion sources are the main drivers of their variability.
- The diurnal variability of BC_{ff} showed an expected double peak (morning/evening) that corresponds to traffic rush hours. BC_{bb} showed a nighttime maximum associated with (potentially unregulated) open biomass burning, which practice is known to occur during the night. Both fossil fuel and biomass burning sources were attributed to local activities within the Greater Cairo region.
- Dust has been found to be a significant component of PM_1, accounting for an average of 24 % over the 2-month duration of the campaign. During an intense dust event, PM_1 concentration peaked at 150 μg m^{-3}, with dust comprising two-thirds of the PM_1 mass. This result highlights that natural aerosols should be carefully measured and accounted for when characterizing submicron aerosols in (semi-) arid urban environments.
- The most abundant chemical component of PM_1 was ammonium chloride (NH_4Cl), corroborating the highly hygroscopic aerosols observed in certain cases (e.g., high loading periods, pollution events). Its diurnal variability revealed overnight formation due to biomass and waste burning and subsequent accumulation under favorable thermodynamic conditions with lower temperatures and higher relative humidity. The concurrent occurrence of biomass/waste burning is further supported by the strong correlation between NH_4, Cl, and K (known as biomass burning tracer). The diurnal variability of NH_4Cl is consistent with rapid volatilization around noon when RH drops below 40–50 % and aerosol liquid water content diminishes. Conversely, high RH levels were found to promote the condensation of the highly hygroscopic NH_4Cl in PM_1, further amplifying the aerosol liquid water content. This finding, together with the significant number fraction of highly hygroscopic particles, highlights the critical role of NH_4Cl as the principal factor behind the intense PM_1 pollution peaks and associated urban haze observed every morning over Cairo.

The persistent chloride concentrations over a two-decade span suggest minimal progress in mitigating the environmental impact of open biomass/waste burning. The latter emerges as a strong pollution source in Cairo and a major contributor to the city's urban haze. Overall, the findings of this study collectively suggest that Cairo may be experiencing a distinct type of urban haze stemming from the combination of chloride in the fine mode and dust in the coarse mode. Both elements could significantly influence the heterogeneous transformation of atmospheric pollutants, with further health implications to remain undetermined.

CRediT authorship contribution statement

Aliki Christodoulou: Conceptualization, Data curation, Formal analysis, Investigation, Methodology, Resources, Validation, Visualization, Writing – original draft, Writing – review & editing. **Spyros Bezantakos:** Data curation, Formal analysis, Investigation, Methodology, Validation, Visualization, Writing – review & editing. **Efstratios Bourtsoukidis:** Supervision, Writing – review & editing. **Iasonas Stavroulas:** Data curation, Investigation, Methodology. **Michael Pikridas:** Data curation, Investigation, Methodology, Visualization. **Konstantina Oikonomou:** Data curation. **Minas Iakovides:** Data curation. **Salwa K. Hassan:** Data curation, Writing – review & editing. **Mohamed Boraiy:** Data curation, Resources. **Mostafa El-Nazer:** Data curation, Resources. **Ali Wheida:** Data curation, Resources. **Magdy Abdelwahab:** Data curation, Resources. **Roland Sarda-Estève:** Data curation, Resources. **Martin Rigler:** Data curation, Resources. **Giorgos Biskos:** Resources. **Charbel Afif:** Conceptualization, Funding acquisition, Project administration. **Agnes Borbon:** Conceptualization, Funding acquisition, Project administration, Writing – review & editing. **Mihalis Vrekoussis:** Supervision, Writing – review & editing. **Nikos Mihalopoulos:** Supervision, Writing – review & editing. **Stéphane Sauvage:** Conceptualization, Funding acquisition, Project administration, Resources, Supervision, Writing – review & editing. **Jean Sciare:** Conceptualization, Funding acquisition, Project administration, Resources, Supervision, Writing – review & editing.

Declaration of competing interest

The authors declare that they have no known competing financial interests or personal relationships that could have appeared to influence

the work reported in this paper.

Data availability

Data will be made available on request.

Acknowledgments

This study has been supported by the European Union's Horizon 2020 research and innovation programme under grant agreement no. 856612 (EMME-CARE) and by the STDF-AUF-IRD launched in 2016 (POLCAIR 'Air Pollution in Cairo: sources and impact). The authors would also like to thank Professor Stephane Alfaro from LISA (France) for his continuous support.

Appendix A. Supplementary data

Supplementary data to this article can be found online at https://doi.org/10.1016/j.envint.2024.108610.

References

Abbass, R.A., Kumar, P., El-Gendy, A., 2020. Car users exposure to particulate matter and gaseous air pollutants in megacity Cairo. Sustain. Cities Soc. 56, 102090 https://doi.org/10.1016/j.scs.2020.102090.

Abu-Allaban, M., Gertler, A.W., Lowenthal, D.H., 2002. A preliminary apportionment of the sources of ambient PM10, PM2.5, and VOCs in Cairo. Atmos. Environ. 36 (35), 5549–5557. https://doi.org/10.1016/S1352-2310(02)00662-3.

Abu-Allaban, M., Lowenthal, D.H., Gertler, A.W., Labib, M., 2007. Sources of PM10 and PM2.5 in Cairo's ambient air. Environ. Monit. Assess. 133 (1–3), 417–425. https://doi.org/10.1007/s10661-006-9596-8.

Ain, N.U., Qamar, S.U.R., 2021. Particulate matter-induced Cardiovascular dysfunction: a mechanistic insight. Cardiovasc. Toxicol. 21 (7), 505–516. https://doi.org/10.1007/s12012-021-09652-3.

Arias-Pérez, R.D., Taborda, N.A., Gómez, D.M., Narvaez, J.F., Porras, J., Hernandez, J.C., 2020. Inflammatory effects of particulate matter air pollution. Environ. Sci. Pollut. Res. 27 (34), 42390–42404. https://doi.org/10.1007/s11356-020-10574-w.

Bezantakos, S., Barmpounis, K., Giamarelou, M., Bossioli, E., Tombrou, M., Mihalopoulos, N., Eleftheriadis, K., Kalogiros, J., Allan, J.D., Bacak, A., Percival, C. J., Coe, H., Biskos, G., 2013. Chemical composition and hygroscopic properties of aerosol particles over the Aegean Sea. Atmos. Chem. Phys. 13 (22), 11595–11608. https://doi.org/10.5194/acp-13-11595-2013.

Bimenyimana, E., Pikridas, M., Oikonomou, K., Iakovides, M., Christodoulou, A., Sciare, J., Mihalopoulos, N., 2023. Fine aerosol sources at an urban background site in the eastern Mediterranean (Nicosia; Cyprus): insights from offline versus online source apportionment comparison for carbonaceous aerosols. Sci. Total Environ. 164741 https://doi.org/10.1016/j.scitotenv.2023.164741.

Budisulistiorini, S.H., Canagaratna, M.R., Croteau, P.L., Baumann, K., Edgerton, E.S., Kollman, M.S., Ng, N.L., Verma, V., Shaw, S.L., Knipping, E.M., Worsnop, D.R., Jayne, J.T., Weber, R.J., Surratt, J.D., 2014. Intercomparison of an aerosol chemical speciation monitor (ACSM) with ambient fine aerosol measurements in downtown Atlanta. Georgia. *Atmospheric Measurement Techniques* 7 (7), 1929–1941. https://doi.org/10.5194/amt-7-1929-2014.

Cavalli, F., Putaud, J.P., 2010. Toward a standardized thermal-optical protocol for measuring atmospheric organic and elemental carbon: the eusaar protocol. ACS, Division of Environmental Chemistry - Preprints of Extended Abstracts 48 (1), 443–446.

Chen, G., Li, S., Zhang, Y., Zhang, W., Li, D., Wei, X., He, Y., Bell, M.L., Williams, G., Marks, G.B., Jalaludin, B., Abramson, M.J., Guo, Y., 2017. Effects of ambient PM1 air pollution on daily emergency hospital visits in China: an epidemiological study. The Lancet Planetary Health 1 (6), e221–e229. https://doi.org/10.1016/S2542-5196(17)30100-6.

Chen, G., Li, X., Liu, X., Chen, Y., Liang, X., Leng, J., Xu, X., Liao, W., Qiu, Y., Wu, Q., 2020. Global projections of future urban land expansion under shared socioeconomic pathways. Nat. Commun. 11 (1), 537.

Chen, G., Canonaco, F., Tobler, A., Aas, W., Alastuey, A., Allan, J., Atabakhsh, S., Aurela, M., Baltensperger, U., Bougiatioti, A., De Brito, J.F., Ceburnis, D., Chazeau, B., Chebaicheb, H., Daellenbach, K.R., Ehn, M., El Haddad, I., Eleftheriadis, K., Favez, O., Prévôt, A.S.H., 2022a. European aerosol phenomenology − 8: Harmonised source apportionment of organic aerosol using 22 Year-long ACSM/AMS datasets. Environ. Int. 166 (May) https://doi.org/10.1016/j.envint.2022.107325.

Chen, Y., Wang, Y., Nenes, A., Wild, O., Song, S., Hu, D., Liu, D., He, J., Ruiz, L.H., Apte, J.S., Gunthe, S.S., Liu, P., 2022b. Ammonium chloride associated aerosol liquid water enhances haze in Delhi India. Environ. Sci. Tech. https://doi.org/10.1021/acs.est.2c00650.

Cheng, Z., Luo, L., Wang, S., Wang, Y., Sharma, S., Shimadera, H., Wang, X., Bressi, M., de Miranda, R.M., Jiang, J., Zhou, W., Fajardo, O., Yan, N., Hao, J., 2016. Status and characteristics of ambient PM2.5 pollution in global megacities. Environ. Int. 89–90, 212–221. https://doi.org/10.1016/j.envint.2016.02.003.

Christodoulou, A., Stavroulas, I., Vrekoussis, M., Desservettaz, M., Pikridas, M., Bimenyimana, E., Kushta, J., Ivančič, M., Rigler, M., Goloub, P., Oikonomou, K., Sarda-Estève, R., Savvides, C., Afif, C., Mihalopoulos, N., Sauvage, S., Sciare, J., 2023. Ambient carbonaceous aerosol levels in Cyprus and the role of pollution transport from the Middle East. Atmos. Chem. Phys. 23 (11), 6431–6456. https://doi.org/10.5194/acp-23-6431-2023.

Clarisse, L., Clerbaux, C., Dentener, F., Hurtmans, D., Coheur, P.F., 2009. Global ammonia distribution derived from infrared satellite observations. Nat. Geosci. 2 (7), 479–483. https://doi.org/10.1038/ngeo551.

Ding, A.J., Huang, X., Nie, W., Sun, J.N., Kerminen, V., Petäjä, T., Su, H., Cheng, Y.F., Yang, X., Wang, M.H., 2016. Enhanced haze pollution by black carbon in megacities in China. Geophys. Res. Lett. 43 (6), 2873–2879.

Dockery, D., Pope, A. (1996). *Epidemiology of acute health effects*.

Drinovec, L., Močnik, G., Zotter, P., Prévôt, A.S.H., Ruckstuhl, C., Coz, E., Rupakheti, M., Sciare, J., Müller, T., Wiedensohler, A., Hansen, A.D.A., 2015. The "dual-spot" aethalometer: an improved measurement of aerosol black carbon with real-time loading compensation. Atmos. Meas. Tech. 8 (5), 1965–1979. https://doi.org/10.5194/amt-8-1965-2015.

El-Metwally, M., Alfaro, S.C., Abdel Wahab, M., Chatenet, B., 2008. Aerosol characteristics over urban Cairo: seasonal variations as retrieved from sun photometer measurements. J. Geophys. Res. Atmos. 113 (14), 1–13. https://doi.org/10.1029/2008JD009834.

El-Metwally, M., Alfaro, S.C., Wahab, M.M.A., Favez, O., Mohamed, Z., Chatenet, B., 2011. Aerosol properties and associated radiative effects over Cairo (Egypt). Atmos. Res. 99 (2), 263–276. https://doi.org/10.1016/j.atmosres.2010.10.017.

ElSaid, S., Aghezzaf, E.-H., 2018. A progress indicator-based assessment guide for integrated municipal solid-waste management systems. J. Mater. Cycles Waste Manage. 20, 850–863.

European Environmental Agency. (2023). *Europe's air quality status 2023* (Briefing no. 05/2023). 10.2800/59526.

Favez, O., Cachier, H., Sciare, J., Alfaro, S.C., El-Araby, T.M., Harhash, M.A., Abdelwahab, M.M., 2008. Seasonality of major aerosol species and their transformations in Cairo megacity. Atmos. Environ. 42 (7), 1503–1516. https://doi.org/10.1016/j.atmosenv.2007.10.081.

Franck, U., Odeh, S., Wiedensohler, A., Wehner, B., Herbarth, O., 2011. The effect of particle size on cardiovascular disorders—the smaller the worse. Sci. Total Environ. 409 (20), 4217–4221.

Friese, E., Ebel, A., 2010. Temperature dependent thermodynamic model of the system H +-NH4+-Na+-SO42-NO3-Cl–H2O. J. Phys. Chem. A 114 (43), 11595–11631. https://doi.org/10.1021/jp101041j.

Gani, S., Bhandari, S., Seraj, S., Wang, D.S., Patel, K., Soni, P., Arub, Z., Habib, G., Hildebrandt Ruiz, L., Apte, J.S., 2019. Submicron aerosol composition in the world's most polluted megacity: the Delhi aerosol supersite study. Atmos. Chem. Phys. 19 (10), 6843–6859. https://doi.org/10.5194/acp-19-6843-2019.

Gerasopoulos, E., Kouvarakis, G., Vrekoussis, M., Donoussis, C., Mihalopoulos, N., Kanakidou, M., 2006. Photochemical ozone production in the eastern Mediterranean. Atmos. Environ. 40 (17), 3057–3069. https://doi.org/10.1016/j.atmosenv.2005.12.061.

Goetz, J.D., Giordano, M.R., Stockwell, C.E., Christian, T.J., Maharjan, R., Adhikari, S., DeCarlo, P.F., 2018. Speciated online PM 1 from south asian combustion sources–part 1: fuel-based emission factors and size distributions. Atmos. Chem. Phys. 18 (19), 14653–14679.

Gunthe, S.S., Liu, P., Panda, U., Raj, S.S., Sharma, A., Darbyshire, E., Reyes-Villegas, E., Allan, J., Chen, Y., Wang, X., Song, S., Pöhlker, M.L., Shi, L., Wang, Y., Kommula, S. M., Liu, T., Ravikrishna, R., McFiggans, G., Mickley, L.J., Coe, H., 2021. Enhanced aerosol particle growth sustained by high continental chlorine emission in India. Nat. Geosci. 14 (2), 77–84. https://doi.org/10.1038/s41561-020-00677-x.

Hassan, S.K., El-Abssawy, A.A., Khoder, M.I., 2013. Characteristics of gas-phase nitric acid and ammonium-nitrate-sulfate aerosol, and their gas-phase precursors in a suburban area in Cairo Egypt. *Atmos. Pollut. Res.* 4 (1), 117–129. https://doi.org/10.5094/APR.2013.012.

Heger, M., Wheeler, D., Zens, G., Meisner, C., & Bank, W. (2019). Motor Vehicle Density and Air Pollution in Greater Cairo: Fuel Subsidy Removal & Metro Line Extension and their Effect on Congestion and Pollution? 48p. http://documents.worldbank.org/curated/en/987971570048516056/pdf/Motor-Vehicle-Density-and-Air-Pollution-in-Greater-Cairo-Fuel-Subsidy-Removal-and-Metro-Line-Extension-and-their-Effect-on-Congestion-and-Pollution.pdf%0Ahttps://trid.trb.org/view/1657874.

Hinds, W.C., 1999. Aerosol technology: properties, behavior, and measurement of airborne Particles, 2nd ed.,. John Willey & Sons Inc.

Hoornweg, D., Pope, K., 2017. Population predictions for the world's largest cities in the 21st century. Environ. Urban. 29 (1), 195–216.

Hu, D., Chen, J., Ye, X., Li, L., Yang, X., 2011. Hygroscopicity and evaporation of ammonium chloride and ammonium nitrate: relative humidity and size effects on the growth factor. Atmos. Environ. 45 (14), 2349–2355. https://doi.org/10.1016/j.atmosenv.2011.02.024.

Hu, Y., Wu, M., Li, Y., Liu, X., 2022. Influence of PM1 exposure on total and cause-specific respiratory diseases: a systematic review and meta-analysis. Environ. Sci. Pollut. Res. 29 (10), 15117–15126. https://doi.org/10.1007/s11356-021-16536-0.

Huang, X., Ding, A., Wang, Z., Ding, K., Gao, J., Chai, F., Fu, C., 2020. Amplified transboundary transport of haze by aerosol–boundary layer interaction in China. Nat. Geosci. 13 (6), 428–434.

Jung, C.H., Kim, Y.P., Lee, K.W., 2002. Simulation of the influence of coarse mode particles on the properties of fine mode particles. J. Aerosol Sci 33 (8), 1201–1216.

Kanakidou, M., Mihalopoulos, N., Kindap, T., Im, U., Vrekoussis, M., Gerasopoulos, E., Dermitzaki, E., Unal, A., Koçak, M., Markakis, K., Melas, D., Kouvarakis, G., Youssef, A.F., Richter, A., Hatzianastassiou, N., Hilboll, A., Ebojie, F., Wittrock, F., von Savigny, C., Moubasher, H., 2011. Megacities as hot spots of air pollution in the East Mediterranean. In Atmospheric Environment (vol. 45 (6), 1223–1235. https://doi.org/10.1016/j.atmosenv.2010.11.048.

Kaskaoutis, D.G., Liakakou, E., Grivas, G., Gerasopoulos, E., Mihalopoulos, N., Alastuey, A., Dulac, F., Dumka, U.C., Pandolfi, M., Pikridas, M., 2023. In: Interannual Variability and Long-Term Trends of Aerosols above the Mediterranean. Springer, pp. 357–390.

Kelly, F.J., Fussell, J.C., 2012. Size, source and chemical composition as determinants of toxicity attributable to ambient particulate matter. Atmos. Environ. 60, 504–526. https://doi.org/10.1016/j.atmosenv.2012.06.039.

Khoder, M.I., 2002. Atmospheric conversion of sulfur dioxide to particulate sulfate and nitrogen dioxide to particulate nitrate and gaseous nitric acid in an urban area. Chemosphere 49 (6), 675–684. https://doi.org/10.1016/S0045-6535(02)00391-0.

Kleanthous, S., Vrekoussis, M., Mihalopoulos, N., Kalabokas, P., Lelieveld, J., 2014. On the temporal and spatial variation of ozone in Cyprus. Sci. Total Environ. 476–477, 677–687. https://doi.org/10.1016/j.scitotenv.2013.12.101.

Kulmala, M., Kokkonen, T.V., Pekkanen, J., Paatero, S., Petäjä, T., Kerminen, V.-M., Ding, A., 2021. Opinion: gigacity–a source of problems or the new way to sustainable development. Atmos. Chem. Phys. 21 (10), 8313–8322.

Lelieveld, J., Berresheim, H., Borrmann, S., Crutzen, P.J., Dentener, F.J., Fischer, H., Feichter, J., Flatau, P.J., Heland, J., Holzinger, R., Korrmann, R., Lawrence, M.G., Levin, Z., Markowicz, K.M., Mihalopoulos, N., Minikin, A., Ramanathan, V., De Reus, M., Roelofs, G.J., Ziereis, H., 2002. Global air pollution crossroads over the mediterranean. Science 298 (5594), 794–799. https://doi.org/10.1126/science.1075457.

Lelieveld, J., Klingmüller, K., Pozzer, A., Pöschl, U., Fnais, M., Daiber, A., Münzel, T., 2019. Cardiovascular disease burden from ambient air pollution in Europe reassessed using novel hazard ratio functions. Eur. Heart J. 40 (20), 1590–1596. https://doi.org/10.1093/eurheartj/ehz135.

Lin, H., Tao, J., Du, Y., Liu, T., Qian, Z., Tian, L., Di, Q., Rutherford, S., Guo, L., Zeng, W., 2016. Particle size and chemical constituents of ambient particulate pollution associated with cardiovascular mortality in Guangzhou, China. Environ. Pollut. 208, 758–766.

Liu, P.S.K., Deng, R., Smith, K.A., Williams, L.R., Jayne, J.T., Canagaratna, M.R., Moore, K., Onasch, T.B., Worsnop, D.R., Deshler, T., 2007. Transmission efficiency of an aerodynamic focusing lens system: comparison of model calculations and laboratory measurements for the aerodyne aerosol mass spectrometer. Aerosol Sci. Tech. 41 (8), 721–733. https://doi.org/10.1080/02786820701422278.

Lowenthal, D.H., Gertler, A.W., Labib, M.W., 2013. Particulate matter source apportionment in cairo : recent measurements and comparison with previous studies. Int. J. Environ. Sci. Technol. https://doi.org/10.1007/s13762-013-0272-6.

Mahmoud, K.F., Alfaro, S.C., Favez, O., Abdel Wahab, M.M., Sciare, J., 2008. Origin of black carbon concentration peaks in Cairo (Egypt). Atmos. Res. 89 (1–2), 161–169. https://doi.org/10.1016/j.atmosres.2008.01.004.

Malm, W.C., Sisler, J.F., Huffman, D., Eldred, R.A., Cahill, T.A., 1994. Spatial and seasonal trends in particle concentration and optical extinction in the United States. J. Geophys. Res. 99 (D1), 1347–1370. https://doi.org/10.1029/93JD02916.

Marey, H.S., Gille, J.C., El-Askary, H.M., Shalaby, E.A., El-Raey, M.E., 2010. Study of the formation of the "black cloud" and its dynamics over Cairo, Egypt, using MODIS and MISR sensors. J. Geophys. Res. Atmos. 115 (21), 1–10. https://doi.org/10.1029/2010JD014384.

Martinelli, N., Olivieri, O., Girelli, D., 2013. Air particulate matter and cardiovascular disease: a narrative review. Eur. J. Intern. Med. 24 (4), 295–302. https://doi.org/10.1016/j.ejim.2013.04.001.

Middlebrook, A.M., Bahreini, R., Jimenez, J.L., Canagaratna, M.R., 2012. Evaluation of composition-dependent collection efficiencies for the aerodyne aerosol mass spectrometer using field data. Aerosol Sci. Tech. 46 (3), 258–271. https://doi.org/10.1080/02786826.2011.620041.

Monged, M. H. E., Imam, N. G., Aquilanti, G., Pollastri, S. (2022). *Heavy metals concentrations and speciation of Pb and Ni in airborne particulate matter over two residential sites in Greater Cairo – reflection from synchrotron radiation research papers.* 765–774. 10.1107/S1600577522003058.

Mostafa, A.N., Wheida, A., El Nazer, M., Adel, M., El Leithy, L., Siour, G., Coman, A., Borbon, A., Magdy, A.W., Omar, M., Saad-Hussein, A., Alfaro, S.C., 2019. Past (1950–2017) and future (−2100) temperature and precipitation trends in Egypt. Weather Clim. Extremes 26, 100225. https://doi.org/10.1016/j.wace.2019.100225.

Nakat, Z., Herrera, S., Cherkaoui, Y., 2013. Cairo traffic congestion study. Addressing Climate Change in the Middle East and North Africa (MENA) Region.

Ng, N.L., Herndon, S.C., Trimborn, A., Canagaratna, M.R., Croteau, P.L., Onasch, T.B., Sueper, D., Worsnop, D.R., Zhang, Q., Sun, Y.L., Jayne, J.T., 2011. An aerosol chemical speciation monitor (ACSM) for routine monitoring of the composition and mass concentrations of ambient aerosol. Aerosol Sci. Tech. 45 (7), 780–794. https://doi.org/10.1080/02786826.2011.560211.

Osipov, S., Chowdhury, S., Crowley, J.N., Tadic, I., Drewnick, F., Borrmann, S., Eger, P., Fachinger, F., Fischer, H., Predybaylo, E., Fnais, M., Harder, H., Pikridas, M., Vouterakos, P., Pozzer, A., Sciare, J., Ukhov, A., Stenchikov, G.L., Williams, J., Lelieveld, J., 2022. Severe atmospheric pollution in the Middle East is attributable to anthropogenic sources. Communications Earth and Environment 3 (1), 1–10. https://doi.org/10.1038/s43247-022-00514-6.

Pant, P., Shukla, A., Kohl, S.D., Chow, J.C., Watson, J.G., Harrison, R.M., 2015. Characterization of ambient PM2.5 at a pollution hotspot in New Delhi, India and inference of sources. Atmos. Environ. 109, 178–189. https://doi.org/10.1016/j.atmosenv.2015.02.074.

Petters, M.D., Kreidenweis, S.M., 2007. A single parameter representation of hygroscopic growth and cloud condensation nucleus activity. Atmos. Chem. Phys. 7 (8), 1961–1971.

Pikridas, M., Vrekoussis, M., Sciare, J., Kleanthous, S., Vasiliadou, E., Kizas, C., Savvides, C., Mihalopoulos, N., 2018. Spatial and temporal (short and long-term) variability of submicron, fine and sub-10 μm particulate matter (PM1, PM2.5, PM10) in Cyprus. Atmos. Environ. 191 (April), 79–93. https://doi.org/10.1016/j.atmosenv.2018.07.048.

Pisso, I., Sollum, E., Grythe, H., Kristiansen, N.I., Cassiani, M., Eckhardt, S., Arnold, D., Morton, D., Thompson, R.L., Groot Zwaaftink, C.D., Evangeliou, N., Sodemann, H., Haimberger, L., Henne, S., Brunner, D., Burkhart, J.F., Fouilloux, A., Brioude, J., Philipp, A., Stohl, A., 2019. The lagrangian particle dispersion model FLEXPART version 10.4. Geosci. Model Dev. 12 (12), 4955–4997. https://doi.org/10.5194/gmd-12-4955-2019.

Prasad, A.K., El-Askary, H., Kafatos, M., 2010. Implications of high altitude desert dust transport from Western Sahara to Nile Delta during biomass burning season. Environ. Pollut. 158 (11), 3385–3391. https://doi.org/10.1016/j.envpol.2010.07.035.

Rader, D.J., McMurry, P.H., 1986. Application of the tandem differential mobility analyzer to studies of droplet growth or evaporation. J. Aerosol Sci 17 (5), 771–787. https://doi.org/10.1016/0021-8502(86)90031-5.

Ramaswami, A., Russell, A.G., Culligan, P.J., Sharma, K.R., Kumar, E., 2016. Meta-principles for developing smart, sustainable, and healthy cities. Science 352 (6288), 940–943.

Reyes-Villegas, E., Panda, U., Darbyshire, E., Cash, J.M., Joshi, R., Langford, B., Di Marco, C.F., Mullinger, N.J., Alam, M.S., Crilley, L.R., Rooney, D.J., Acton, W.J.F., Drysdale, W., Nemitz, E., Flynn, M., Voliotis, A., McFiggans, G., Coe, H., Lee, J., Allan, J.D., 2021. PM1 composition and source apportionment at two sites in Delhi, India, across multiple seasons. Atmos. Chem. Phys. 21 (15), 11655–11667. https://doi.org/10.5194/acp-21-11655-2021.

Saarikoski, S., Carbone, S., Decesari, S., Giulianelli, L., Angelini, F., Teinilä, K., Canagaratna, M., Ng, N. L., Trimborn, A., Facchini, M. C., Fuzzi, S., Hillamo, R., Worsnop, D. (2012). Corrigendum to "Chemical characterization of springtime submicrometer aerosol in Po Valley, Italy" published in Atmos. Chem. Phys., 12, 8401–8421, 2012. *Atmospheric Chemistry and Physics*, *12*(18), 8633. 10.5194/acp-12-8633-2012.

Saha, S., Moorthi, S., Wu, X., Wang, J., Nadiga, S., Tripp, P., Behringer, D., Hou, Y.-T., Chuang, H., Iredell, M., 2014. The NCEP climate forecast system version 2. J. Clim. 27 (6), 2185–2208.

Salmatonidis, A., Viana, M., Biskos, G., Bezantakos, S., 2020. Particle size distributions and hygroscopic restructuring of ultrafine particles emitted during thermal spraying. Aerosol Sci. Tech. 54 (12), 1359–1372. https://doi.org/10.1080/02786826.2020.1784837.

Sandradewi, J., Prévôt, A.S.H., Szidat, S., Perron, N., Alfarra, M.R., Lanz, V.A., Weingartner, E., Baltensperger, U.R.S., 2008. Using aerosol light abosrption measurements for the quantitative determination of wood burning and traffic emission contribution to particulate matter. Environ. Sci. Tech. 42 (9), 3316–3323. https://doi.org/10.1021/es702253m.

Sciare, J., Cachier, H., Sarda-Estève, R., Yu, T., Wang, X., 2007. Semi-volatile aerosols in Beijing (RP China): Characterization and influence on various PM2. 5 measurements. J. Geophys. Res. Atmos. 112 (D18).

Sciare, J., Sarda-Estève, R., Favez, O., Cachier, H., Aymoz, G., Laj, P., 2008. Nighttime residential wood burning evidenced from an indirect method for estimating real-time concentration of particulate organic matter (POM). Atmos. Environ. 42 (9), 2158–2172. https://doi.org/10.1016/j.atmosenv.2007.11.053.

Simon, H., Bhave, P.V., Swall, J.L., Frank, N.H., Malm, W.C., 2011. Determining the spatial and seasonal variability in OM/OC ratios across the US using multiple regression. Atmos. Chem. Phys. 11 (6), 2933–2949.

Stavroulas, I., Bougiatioti, A., Grivas, G., Paraskevopoulou, D., Tsagkaraki, M., Zarmpas, P., Liakakou, E., Gerasopoulos, E., Mihalopoulos, N., 2019. Sources and processes that control the submicron organic aerosol composition in an urban Mediterranean environment (Athens): a high temporal-resolution chemical composition measurement study. Atmos. Chem. Phys. 19 (2), 901–919. https://doi.org/10.5194/acp-19-901-2019.

Stohl, A., Eckhardt, S., Forster, C., James, P., Spichtinger, N., 2002. On the pathways and timescales of intercontinental air pollution transport. J. Geophys. Res. Atmos. 107 (D23), ACH-6. https://doi.org/10.1029/2001JD001396.

Stolzenburg, M.R., McMurry, P.H., 1991. An ultrafine aerosol condensation nucleus counter. Aerosol Sci. Tech. 14 (1), 48–65. https://doi.org/10.1080/02786829108959470.

Sun, C., Lee, B.P., Huang, D., Jie Li, Y., Schurman, M.I., Louie, P.K.K., Luk, C., Chan, C.K., 2016. Continuous measurements at the urban roadside in an asian megacity by aerosol chemical speciation monitor (ACSM): particulate matter characteristics during fall and winter seasons in Hong Kong. Atmos. Chem. Phys. 16 (3), 1713–1728. https://doi.org/10.5194/acp-16-1713-2016.

Sun, Y., Wang, Z., Dong, H., Yang, T., Li, J., Pan, X., Chen, P., Jayne, J.T., 2012. Characterization of summer organic and inorganic aerosols in Beijing, China with an aerosol chemical speciation monitor. Atmos. Environ. 51, 250–259.

Swietlicki, E., Hansson, H.C., Hämeri, K., Svenningsson, B., Massling, A., Mcfiggans, G., Mcmurry, P.H., Petäjä, T., Tunved, P., Gysel, M., Topping, D., Weingartner, E., Baltensperger, U., Rissler, J., Wiedensohler, A., Kulmala, M., 2008. Hygroscopic properties of submicrometer atmospheric aerosol particles measured with H-TDMA instruments in various environments - a review. Tellus B Chem. Phys. Meteorol. 60 (B(3)), 432–469. https://doi.org/10.1111/j.1600-0889.2008.00350.x.

The World Bank Group. (n.d.). *Egypt – Climatology*. Retrieved February 23, 2024, from https://climateknowledgeportal.worldbank.org/country/egypt/climate-data-historical.

Tsai, I., Chen, J., Lin, Y., Chou, C.C., Chen, W., 2015. Numerical investigation of the coagulation mixing between dust and hygroscopic aerosol particles and its impacts. J. Geophys. Res. Atmos. 120 (9), 4213–4233.

Van Damme, M., Clarisse, L., Whitburn, S., Hadji-Lazaro, J., Hurtmans, D., Clerbaux, C., Coheur, P.F., 2018. Industrial and agricultural ammonia point sources exposed. Nature 564 (7734), 99–103. https://doi.org/10.1038/s41586-018-0747-1.

Vrekoussis, M., Liakakou, E., Koçak, M., Kubilay, N., Oikonomou, K., Sciare, J., Mihalopoulos, N., 2005. Seasonal variability of optical properties of aerosols in the eastern mediterranean. Atmos. Environ. 39 (37), 7083–7094. https://doi.org/10.1016/j.atmosenv.2005.08.011.

Vrekoussis, M., Pikridas, M., Rousogenous, C., Christodoulou, A., Desservettaz, M., Sciare, J., Richter, A., Bougoudis, I., Savvides, C., Papadopoulos, C., 2022. Local and regional air pollution characteristics in Cyprus: a long-term trace gases observations analysis. Sci. Total Environ. 845, 157315 https://doi.org/10.1016/j.scitotenv.2022.157315.

Wang, S.C., Flagan, R.C., 1989. Scanning electrical mobility spectrometer. J. Aerosol Sci 20 (8), 1485–1488. https://doi.org/10.1016/0021-8502(89)90868-9.

Wang, Z., Huang, X., Ding, A., 2018. Dome effect of black carbon and its key influencing factors: a one-dimensional modelling study. Atmos. Chem. Phys. 18 (4), 2821–2834.

Wexler, A.S., Clegg, S.L., 2002. Atmospheric aerosol models for systems including the ions H+, NH4+, Na+, so42-, NO 3-, Cl-, Br-, and H2O. J. Geophys. Res. Atmos. 107 (14), ACH-14. https://doi.org/10.1029/2001JD000451.

Witz, S., Eden, R.W., Wadley, M.W., Dunwoody, C., Papa, R.P., Torre, K.J., 1990. Rapid loss of particulate nitrate, chloride and ammonium on quartz fiber filters during storage. J. Air Waste Manag. Assoc. 40 (1), 53–61. https://doi.org/10.1080/10473289.1990.10466666.

World Development Indicators 2012, The World Bank, 10.1596/978-0-8213-8985-0, 2012.

World Health Organization. (2021). WHO global air quality guidelines: particulate matter (PM2.5 and PM10), ozone, nitrogen dioxide, sulfur dioxide and carbon monoxide. World Health Organization. https://iris.who.int/handle/10665/345329. License: CC BY-NC-SA 3.0 IGO.

Zakey, A.S., Abdel-Wahab, M.M., PETTERSSON, J.B.C., Gatari, M.J., Hallquist, M., 2008. Seasonal and spatial variation of atmospheric particulate matter in a developing megacity, the greater Cairo. Egypt. *Atmosfera* 21 (2), 171–189.

Zhang, B., Shen, H., Yun, X., Zhong, Q., Henderson, B.H., Wang, X., Shi, L., Gunthe, S.S., Huey, L.G., Tao, S., Russell, A.G., Liu, P., 2022. Global emissions of hydrogen chloride and particulate chloride from continental sources. Environ. Sci. Tech. 56 (7), 3894–3904. https://doi.org/10.1021/acs.est.1c05634.

Zhou, W., Wang, Q., Zhao, X., Xu, W., Chen, C., Du, W., Zhao, J., Canonaco, F., Prévôt, A. S.H., Fu, P., Wang, Z., Worsnop, D.R., Sun, Y., 2018. Characterization and source apportionment of organic aerosol at 260gm on a meteorological tower in Beijing China. *Atmos. Chem. Phys.* 18 (6), 3951–3968. https://doi.org/10.5194/acp-18-3951-2018.

Zittis, G., Hadjinicolaou, P., Klangidou, M., Proestos, Y., Lelieveld, J., 2019. A multi-model, multi-scenario, and multi-domain analysis of regional climate projections for the Mediterranean. Reg. Environ. Chang. 19 (8), 2621–2635. https://doi.org/10.1007/s10113-019-01565-w.

Zittis, G., Almazroui, M., Alpert, P., Ciais, P., Cramer, W., Dahdal, Y., Fnais, M., Francis, D., Hadjinicolaou, P., Howari, F., Jrrar, A., Kaskaoutis, D.G., Kulmala, M., Lazoglou, G., Mihalopoulos, N., Lin, X., Rudich, Y., Sciare, J., Stenchikov, G., Lelieveld, J., 2022. Climate change and weather extremes in the eastern Mediterranean and Middle East. Rev. Geophys. 60 (3) https://doi.org/10.1029/2021rg000762.